

Single-shot imaging with randomized structured illumination at a free electron laser

ABRAHAM L. LEVITAN,^{1,2*} KAHRAMAN KESKINBORA,¹ MATTEO PANCALDI,^{3,4} DIETER W. ENGEL,⁵ EMANUELE PEDERSOLI,³ FLAVIO CAPOTONDI,³ AND RICCARDO COMIN¹

¹*Massachusetts Institute of Technology, 77 Mass Avenue, Cambridge, MA 02139, USA*

²*Paul Scherrer Institute, Forschungsstrasse 111, 5232 Villigen PSI, Switzerland*

³ *Elettra-Sincrotrone Trieste, Strada Statale 14 km 163,5 in Area Science Park, I-34012 Basovizza, Trieste, Italy*

⁴*Department of Molecular Sciences and Nanosystems, Ca' Foscari University of Venice, I-30172 Venezia Mestre, Italy*

⁵*Max-Born-Institut für Nichtlineare Optik und Kurzzeitspektroskopie, Max-Born-Straße 2A, 12489 Berlin, Germany*

*alevitan@mit.edu

Abstract: Stroboscopic nanoscale imaging with free electron laser light is revolutionizing our understanding of fast dynamics in heterogeneous systems. The short wavelength of X-ray and extreme ultraviolet radiation makes it possible to achieve nanoscale resolution, while resonance with atomic transitions gives access to electronic and magnetic degrees of freedom. Here, we report on our implementation of a recently developed imaging method, randomized probe imaging, at a free electron laser. The advantage of randomized probe imaging over existing methods is its compatibility both with extended and strongly scattering samples. Our implementation delivers robust single-shot reconstructions at up to a full-pitch resolution of 400 nm over a field of view with a 40 μm diameter. We also demonstrate single-shot imaging of magnetic domain structures using circular dichroism at resonance, paving the way to future time-resolved studies of magnetic dynamics, shock physics, and the dynamics of collective electronic phases.

1. Introduction

Following the 2006 experiment performed by Chapman et al [1], X-ray coherent diffraction imaging (CDI) [2, 3] has been used at free electron lasers (FELs) to image an astonishing variety of phenomena. A program of research that began by imaging simple test objects [1, 4] was soon studying the morphology of metallic nanoparticles [5–7], soot [8, 9], helium nanodroplets [10], battery electrolytes [11], viruses [12, 13], organelles [14–16], and even whole bacterial cells [17–19].

The introduction of other, related quantitative phase imaging methods at FELs broadened the possibilities further. For example, taking in-line holography (ILH) [20, 21] data—which can then be analyzed with various algorithms [22–25]—enables experimenters to work with extended (i.e. non-isolated) samples. ILH has therefore been very useful for visualizing the mechanical properties of matter undergoing rapid changes, e.g. propagating shock waves [26–29], cavitation bubbles [24], liquid microjets [25], and exploding capillaries [30].

Going in a different direction, Fourier transform holography (FTH) [31, 32] and its derivatives [33–35] introduce extra sample masking and preparation steps but produce data which can be reconstructed more reliably, and with less computational cost, than either CDI or ILH data can. This is especially true when the sample is a strong scatterer or contains densely packed features, both of which would destabilize an ILH reconstruction. For this reason, FTH has become popular for studies using extreme ultraviolet and soft X-ray light, where the strong resonant coupling to electronic degrees of freedom has enabled studies of magnetism in thin films [36, 37], including picosecond-scale dynamics [38].

For quantitative phase imaging at an FEL today, one can choose to either image an extended sample or a strongly scattering sample, but not both at once. As a result, for phase imaging there is no standard FEL-based method with the same robustness and simplicity as FEL-based full-field absorption contrast imaging [39]. This is the motivation behind our FEL-based implementation of randomized probe imaging (RPI), a quantitative phase imaging method that works reliably with extended, strongly scattering samples [40].

The ability to work in the same regime of quality and resolution as existing methods, which we demonstrate with a comprehensive literature search, is the main distinction between RPI and the exciting recent report of an FEL based implementation of single-shot ptychography (SSP) [41, 42]. Furthermore, RPI is robust, with a well-posed inverse problem that rapidly converges even on complicated samples. The experiment itself is simple and can be done at nearly any coherent X-ray scattering instrument which supports ptychography. No optics need to be placed in the Fresnel regime of the sample, creating space for special sample environments and optical photoexcitation. Finally, RPI is scalable: the inverse problem remains well-posed even if a large field of view is imaged in high resolution [40].

In the experiment reported here we show that these advantages carry over from the synchrotron to the FEL context, enabling single-shot imaging of both structural and magnetic samples. On the structural front, we reconstruct complex-valued images of Siemens star test samples, enabling us to assess the quality of our RPI results in detail and explore the prospects for future implementations. In addition, we report images of magnetic domain structures in a thin Pt/Co/Ta multilayer sample, demonstrating the basic applicability of the method to challenging samples with weak contrast. In sum, RPI's unique combination of advantages makes it a compelling alternative to CDI, ILH, and FTH for a variety of experiments across the wavelength range used at FELs.

2. Methods

The workflow that we established for single-shot FEL-based RPI experiments is shown in Figure 1a. A single FEL pulse passes through a randomized zone plate (RZP) [40] (Figure 1b), which projects a speckled structured illumination function (Figure 1c) onto the sample. The upstream optics at the beamline are set to overfill the RZP by several times, helping to mitigate the shot-to-shot wavefront instability of the FEL. Further information on the design and fabrication of this optic is found in supplemental section S1. In this work, we first used a roughly 60 fs long pulse of 20.8 nm wavelength light produced by the FERMI FEL to image a gold Siemens star (Figure 1d) on a 30 nm thick silicon nitride window. After passing through the sample, the light propagates to the far field where the diffracted intensity is recorded on a detector. A typical raw single-shot pattern, consisting of approximately 1.2×10^7 measured photons and arising from an estimated incident pulse energy at the sample plane of 1.4 nJ, is shown in Figure 1e. Further information about the detailed experimental setup is found in supplemental section S2.

Detailed knowledge of the illumination wavefield is obtained empirically by reconstructing a standard transmission ptychography dataset [43] collected with one shot per exposure on a static sample. Here, this ptychography reconstruction was performed with the `cdtools` package [44] using an automatic differentiation-based reconstruction algorithm which included 3 incoherently mixing probe modes [45], probe position refinement with a gradient-based algorithm [46], a shot-to-shot total intensity factor, a frame-independent detector background model [47], and a super-resolution approach inspired by [48]. The exact details of the reconstruction algorithm can be found in the publicly available replication data and code for this work [49]. Super-resolution was used to avoid aliasing artifacts because the scattered intensity remained high at the detector edges.

Using the Fourier ring correlation, we determined that the ptychography reconstruction of the Siemens star target was reliable to the super-resolution pixel pitch of 73 nm, a full-pitch

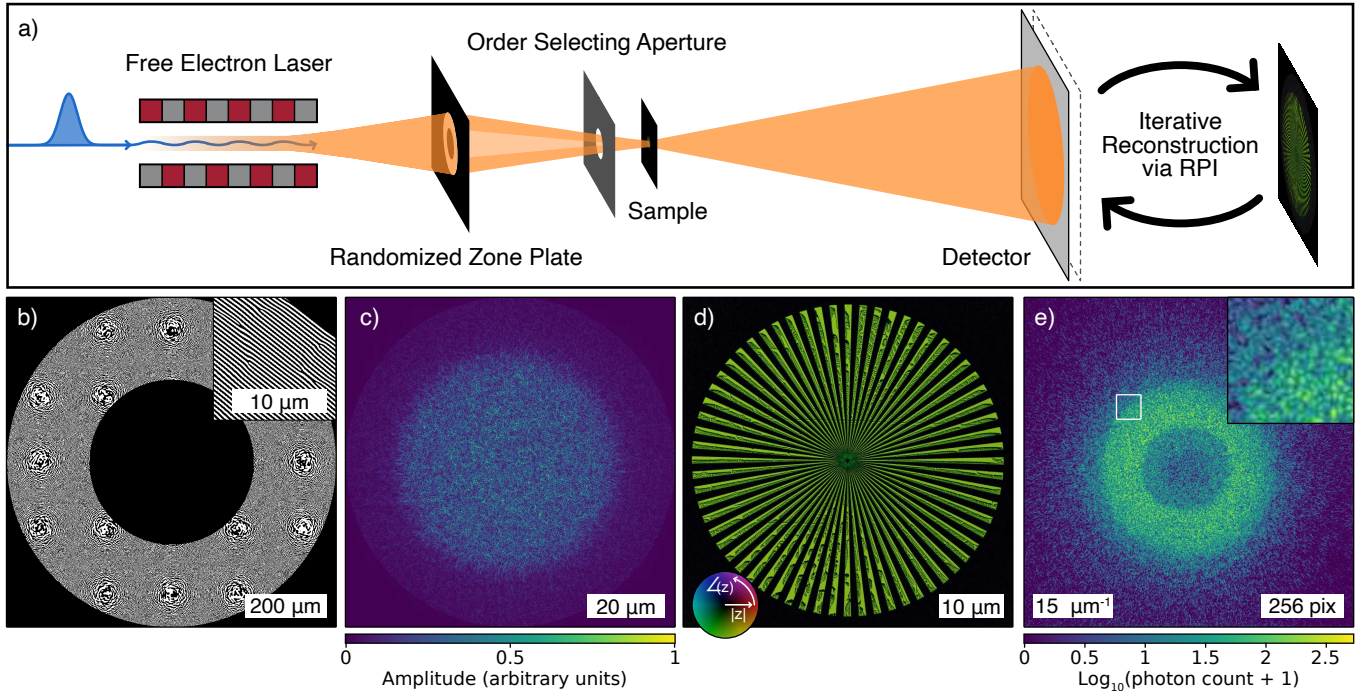


Fig. 1. **Experiment Overview.** (a) A diagram of the experiment’s geometry and workflow. (b) The design file for the optic used in the experiment, sampled in 1 μm steps. Inset: a section of the outer region, showing typical phase defects. (c) The probe function at the sample plane, as retrieved via ptychography. (d) The sample’s complex-valued object function, as retrieved via ptychography. (e) A typical single-shot diffraction pattern, with the inset showing the detailed speckle structure.

resolution of 146 nm. We also established the reliability of the recovered probes, finding a normalized amplitude-minimized partially coherent mean squared error [50] of 9.1% between probes recovered from each half of the dataset. Various additional assessments of the recovered ptychography quality are shown in supplementary Figure S4.

Following this calibration step, the probe function recovered from ptychography is used in conjunction with the RPI algorithm [40] to reconstruct images of the illuminated region of the Siemens star test object on a shot-to-shot basis. This algorithm, described in full in [40], uses a band-limiting constraint on the object together with knowledge of the illumination function to stabilize the phase retrieval problem. The single-shot RPI reconstructions were performed with the *cdtools* package [44], using 650×650 pixel objects with a pixel size of 160 nm. As discussed in [40], the resolution of the single-shot RPI reconstructions is roughly limited by the length scale of the speckles in the structured illumination, which is ultimately tied to the outer zone width of the RZP. In this work, the optic’s outer zone width was 200 nm, and as we demonstrate next, the design full-pitch resolution of 400 nm was achieved.

3. Results

A typical single-shot RPI reconstruction from this setup is shown in Figures 2a and 2b. Despite the presence of noise, the good subjective visual quality is immediately apparent, as is the lack of obvious artifacts. Furthermore, the reconstructions are remarkably consistent. The image in Figure 2a was inverted from the first of a series of 128 consecutive exposures. The reconstruction

from each of the 128 exposures attained a similar quality level, and all 128 images are presented in supplementary figures S6 and S7.

We evaluated the quality of these images using the spectral signal-to-noise ratio (SSNR) [51], shown in Figure 2e. This was estimated from a Fourier cross resolution curve [51] calculated between the RPI results and an appropriately downsampled ptychography reconstruction of the same sample using the methodology described in supplementary note S4. The resulting curve has a characteristic shape with a dip at intermediate spatial frequencies, due to the lack of these frequencies in the Siemens star test object. To estimate the resolution attained, we compared the SSNR curve with a half-bit threshold of 0.4142 [52], commonly used to assess the resolution of lensless imaging data [53–56]. By this metric, the vast majority of the 128 reconstructions surpassed the design full-pitch resolution of 400 nm, corresponding to the optic’s 200 nm outer zone width. The worst SSNR-determined resolution among the full set of 128 reconstructions was 420 nm.

Each single-shot diffraction pattern contained an average of 1.2×10^7 detected photons, equivalent to 490 photons per 200 nm resolution element within the illuminated region. To understand how the quality of RPI reconstructions would improve as the fluence increases, we averaged the results of subsequent single-shot reconstructions after aligning the images to correct for the roughly 1 μm positioning jitter. An example summed image, generated from 64 reconstructions and 3.1×10^4 photons per resolution element, is shown in Figure 2c and compared to a corresponding ptychography reconstruction shown in Figure 2d.

The SSNR improved as we included more exposures in the summed image, with the quality saturating around 64 exposures. Quantitatively, the normalized mean squared error [57] calculated between summed RPI images and downsampled ptychography images saturated just under 5%. This implies that the quality was ultimately limited by other noise sources, such as the presence of unaccounted-for high spatial frequency components in the object function or potentially insufficient shot-to-shot stability of the illumination wavefield. For a sum of 64 exposures the images were resolved pixel-by-pixel, with an SSNR at the pixel pitch of roughly 3 as shown in Figure 2e.

For a more direct confirmation that the design resolution was achieved in single-shot images, in Figure 2f we used the methodology described in supplementary note S5 to plot a cut from the image along an arc which intersects the spokes of the Siemens star at a 400 nm pitch. The periodic pattern of spokes is clearly resolved, supporting our claim of a 400 nm full-pitch resolution.

Following the imaging experiments with resolution test targets, we assessed the viability of FEL based RPI for resonant imaging of magnetic thin films. To do this, we collected similar ptychography and RPI datasets from a magnetic thin film using circular left- and right-hand illumination at the Co M3 edge. The multilayer thin film was prepared with a nominal structure of Ta(3 nm)/[Pt(3 nm)/Co(1 nm)/Ta(1.9 nm)] \times 10/Pt(2 nm), deposited on a 30 nm thick silicon-rich silicon nitride membrane using direct current and radio frequency magnetron sputtering. During deposition, the argon pressure was adjusted to 4.6×10^{-3} mbar. This preparation hosts natural magnetic domains at remanence, covering a variety of length scales from several hundred nm to several μm .

Ptychography reconstructions with right-hand and left-hand circularly polarized illumination are shown in Figures 3a-3c. The contrast reversal demonstrates the magnetic origin of the imaged structures. The left-hand circular results, which were used to calibrate the RPI reconstructions, achieved a resolution of 390 nm as determined by SSNR. Various standard assessments of the recovered image quality are shown in supplementary figure S5.

A series of 64 shots of RPI data were then captured under left-hand circularly polarized illumination, with a mean of 2.8×10^6 photons measured per shot. RPI reconstructions were performed with a 200×200 pixel object with a pixel size of 520 nm. An example single-shot RPI reconstruction is shown in Figure 3d, and an average of all 64 individual RPI reconstructions

is shown in Figures 3e and 3f. Notably, both amplitude and phase contrast arising from the magnetic domains is visible in the averaged RPI images. SSNR curves calculated via comparison between RPI and ptychography results are shown in Figure 3g, indicating that the single-shot reconstructions achieved a full-pitch resolution of $2.22\ \mu\text{m}$, and averages of 12 or more images achieved the pixel-limited full-pitch resolution of $1.04\ \mu\text{m}$.

Finally, we estimated the space-bandwidth product (SBP) of the single-shot reconstructions. SBP is a measure of the number of individually resolved resolution elements contained within the image [58]. It is defined as the product of the accessible area in real space and reciprocal space:

$$\text{SBP} = A_{\text{real}}A_{\text{Fourier}} = \pi^2 \frac{r^2}{\text{res}^2}. \quad (1)$$

Conservatively estimating our field of view as a $40\ \mu\text{m}$ diameter focal spot, we find a SBP of 2.5×10^4 for the single-shot structural images, 3.6×10^3 for the 64 shot magnetic images, and 8.0×10^2 for the single-shot magnetic images. These are equivalent to a perfectly resolved 160×160 pixel image, 60×60 pixel image, and 28×28 pixel image, respectively.

4. Discussion

We have implemented RPI at an FEL, showing that RPI accommodates noisy conditions gracefully and that it is possible to collect high-quality images with sufficiently high flux. The reliability of the method was demonstrated by the remarkably consistent quality achieved across reconstructions from 128 consecutive exposures. In addition, we demonstrated that the method is sufficiently sensitive to image the X-ray circular magnetic dichroic contrast in magnetic domain structures, albeit at a reduced resolution. Combined with the various other advantages of RPI—a simple experimental geometry, applicability to samples with strong phase and amplitude features, and compatibility with extended samples—this already makes RPI unusual in the world of FEL-based quantitative phase imaging methods. As we discuss next, RPI is also competitive with existing methods for single-shot quantitative phase imaging at FELs when considering metrics for image quality, namely resolution and SBP.

To understand how our implementation compares with the state of the art, we performed a comprehensive literature search to find all published quantitative phase images collected at FELs using methods compatible with single-shot operation, at any wavelength from extreme ultraviolet to hard X-ray. We identified 102 datasets from 97 papers published before November 12, 2023. We estimated the resolution and SBP of the highest-resolution image in each dataset, and organized the images into several groups by imaging method. Our methodology for this literature search is described in supplementary note S5.

The results in Figure 4 reveal RPI's unique capabilities. Clustered in the upper left region of the plot—with high SBP but low resolution—are ILH based studies. Like RPI, ILH works on extended samples, but notably the resolution we achieve is higher than the resolution achieved by any published quantitative phase image from an FEL-based ILH experiment. We note that synchrotron-based ILH experiments in the hard X-ray regime—not covered by this literature review—do routinely achieve resolutions in the tens of nanometers.

In the lower right region of the plot lie most CDI and FTH reconstructions. CDI and FTH can achieve astonishingly high resolutions, however, they are restricted to isolated samples. Further, both methods, especially CDI, are limited in SBP. Therefore, no FEL-based CDI image, and only one FEL-based FTH image [61], has ever reached a higher SBP than that of our recovered images.

The only truly comparable method—both maskless and applicable to strongly scattering samples—that has been used for quantitative phase imaging at an FEL is SSP [42]. The reconstructions from our implementation achieve a far higher resolution and SBP than the current state of the art in FEL-based SSP.

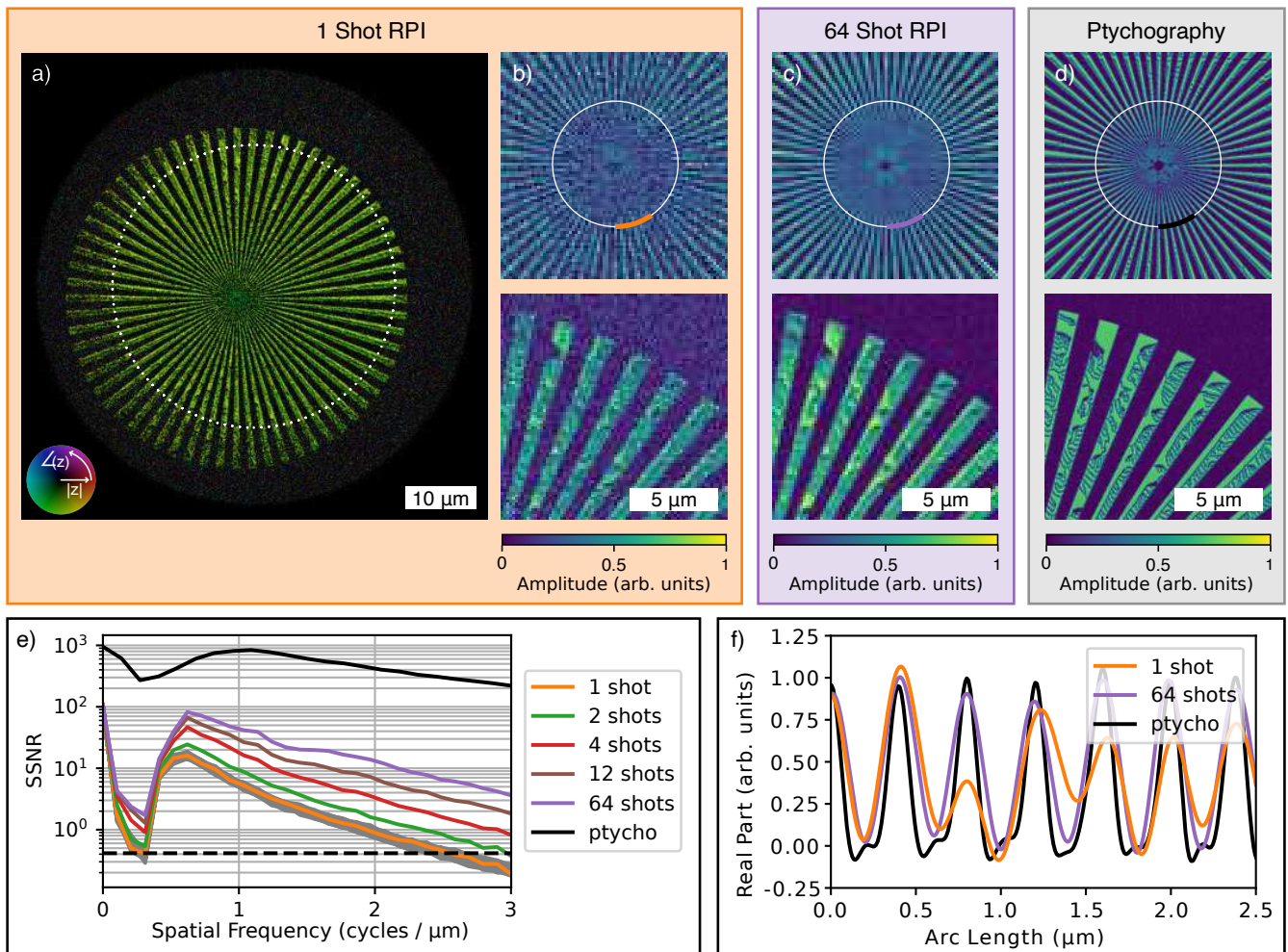


Fig. 2. **RPI Reconstruction.** (a) The complex-valued result of a typical single-shot reconstruction. The approximate illuminated region is outlined with a white dashed line. (b) Top, a closeup of the amplitude within the central region. The white circle intersects the spokes at a 400 nm pitch. Bottom, an outer region of the field of view. (c) The same regions, extracted from the mean of 64 single-shot images. (d) The same regions, extracted from the calibration ptychography reconstruction. (e) The SSNR of the single-shot reconstruction, as well as various summed images and the ptychography reconstruction. The grey lines are the results from all 128 single-shot reconstructions, and the black dashed line indicates the half-bit threshold (f) Line cuts extracted along the paths defined in b,c, and e.

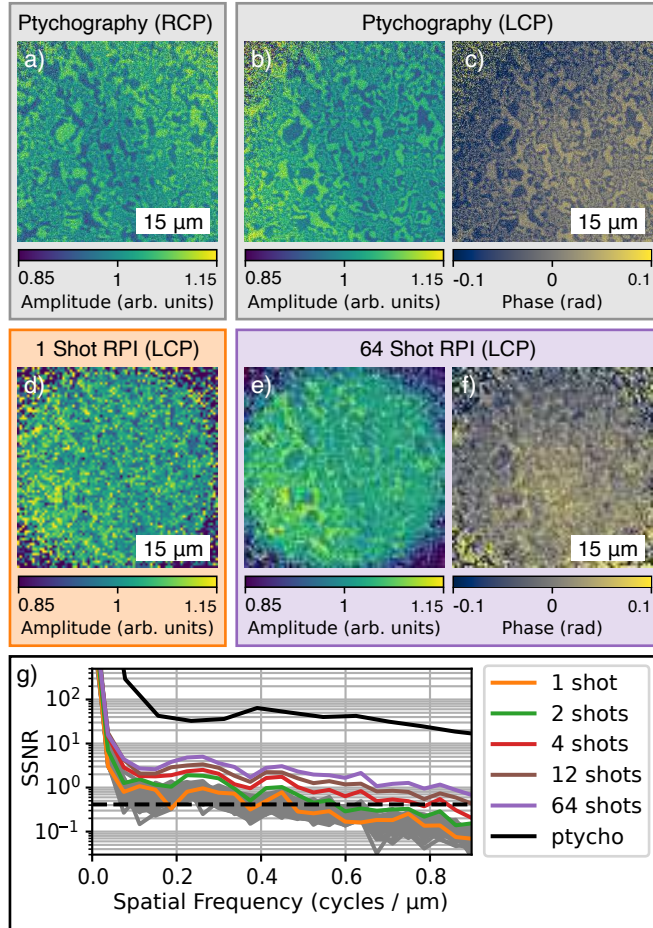


Fig. 3. **Imaging of a magnetic film.** (a) The amplitude of a ptychography reconstruction from a Pt/Co/Ta multilayer under right-hand circularly polarized illumination. The natural magnetic domain structure is visible. (b) The amplitude and (c) phase of a ptychography reconstruction of the same region under left-hand circular illumination. (d) Single-shot RPI from the same region. (e) The amplitude and (f) phase of an average of 64 RPI reconstructions. (g) The SSNR of the ptychography and RPI reconstructions, with varying numbers of summed images. The grey lines are the results from all 64 single-shot reconstructions, and the black dashed line indicates the half-bit threshold.

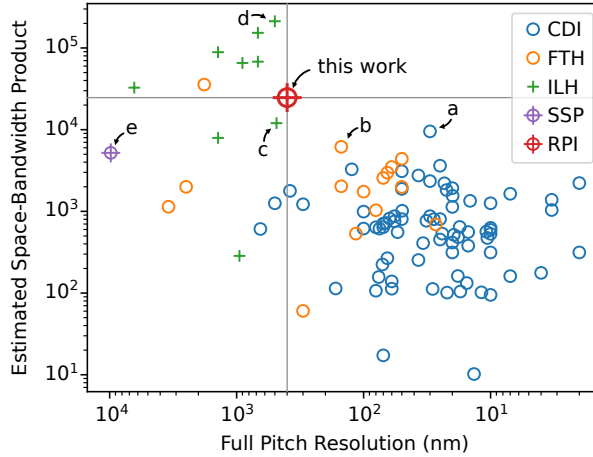


Fig. 4. **Comparison.** A comparison of our single-shot RPI experiment on the gold test structure to all published quantitative phase images collected at FELs using single-shot compatible methods as of November 2023. Circular markers (CDI and FTH) indicate methods which are applicable to strong scatterers. Crosses (ILH) indicate maskless experiments. Methods which have both properties (SSP and RPI) have a combined marker. Several relevant experiments are explicitly labeled, and the reader is encouraged to compare our work to these results to understand the qualitative improvement in visual quality afforded by RPI. a: [59] (Figure 3); b: [60] (Figure 4h); c: [21] (Figure 3); d: [24] (Figure 2d); and e [42] (Figure 4c).

Considering the plot as a whole, our RPI implementation lies on the Pareto frontier of resolution and SBP for FEL-based experiments. Improvements along both axes are also feasible. The half-pitch resolution is ultimately limited by the outer zone width of the RZP used. Zone plates with 20 nm outer zone widths are not uncommon. The SBP is ultimately limited by the detector pixel count, photon budget, and/or the source bandwidth. With current detector and source technologies, we expect that a SBP in excess of 10^5 is achievable.

In summary, RPI can be implemented at a seeded FEL source, and the resulting images are both competitive with state of the art methods and applicable to meaningful samples, such as systems of magnetic domains in extended thin films. We expect that RPI’s simplicity, reliability, and compatibility with unmasked samples will make it an attractive option for many stroboscopic imaging experiments that otherwise would have used FTH, CDI, or ILH.

Funding. This material is based upon work supported by the Department of Energy, Office of Science, Office of Basic Energy Sciences, under Award Number DE-SC0021939. The P6000 GPU used for the reconstructions in this paper was donated by the NVIDIA Corporation. K.K. acknowledges funding support by the German Research Foundation (DFG) under project number 428809035.

Author Contribution Statement.

AL, KK, and RC developed the concept for and organized the experiment. AL and KK designed and KK fabricated the optics. DE grew the magnetic thin film sample. The experiment setup was designed and installed by MP, EP, and FC. AL, KK, MP, EP, and FC participated in data collection. The data analysis, reconstructions, and literature review were performed by AL. All authors contributed to the manuscript.

Acknowledgment. We thank Dr. Yang Yu from Raith US and MIT.nano for his invaluable help with the VELION ion beam lithography instrument.

Disclosures. E: KK now works for Raith Group, which is a supplier of the dedicated IBL system used in

this work.

Data availability. The raw data, analysis scripts, and literature search data used in this paper have been made available at reference [49].

Supplemental document. See Supplement 1 for supporting content.

5. References

References

1. H. N. Chapman, A. Barty, M. J. Bogan, *et al.*, “Femtosecond diffractive imaging with a soft-X-ray free-electron laser,” *Nat. Phys.* **2**, 839–843 (2006).
2. J. R. Fienup, “Reconstruction of a complex-valued object from the modulus of its Fourier transform using a support constraint,” *J. Opt. Soc. Am. A* **4**, 118 (1987).
3. J. Miao, P. Charalambous, J. Kirz, and D. Sayre, “Extending the methodology of X-ray crystallography to allow imaging of micrometre-sized non-crystalline specimens,” *Nature* **400**, 342–344 (1999).
4. A. Barty, S. Boutet, M. J. Bogan, *et al.*, “Ultrafast single-shot diffraction imaging of nanoscale dynamics,” *Nat. Photonics* **2**, 415–419 (2008).
5. Y. Takahashi, A. Suzuki, N. Zettsu, *et al.*, “Coherent Diffraction Imaging Analysis of Shape-Controlled Nanoparticles with Focused Hard X-ray Free-Electron Laser Pulses,” *Nano Lett.* **13**, 6028–6032 (2013).
6. J. N. Clark, L. Beitra, G. Xiong, *et al.*, “Imaging transient melting of a nanocrystal using an X-ray laser,” *Proc. National Acad. Sci.* **112**, 7444–7448 (2015).
7. Y. Ihm, D. H. Cho, D. Sung, *et al.*, “Direct observation of picosecond melting and disintegration of metallic nanoparticles,” *Nat. Commun.* **10**, 2411 (2019).
8. M. J. Bogan, S. Boutet, H. N. Chapman, *et al.*, “Aerosol Imaging with a Soft X-Ray Free Electron Laser,” *Aerosol Sci. Technol.* **44**, i–vi (2010).
9. N. D. Loh, C. Y. Hampton, A. V. Martin, *et al.*, “Fractal morphology, imaging and mass spectrometry of single aerosol particles in flight,” *Nature* **486**, 513–517 (2012).
10. C. F. Jones, C. Bernardo, R. M. P. Tanyag, *et al.*, “Coupled motion of Xe clusters and quantum vortices in He nanodroplets,” *Phys. Rev. B* **93**, 180510 (2016).
11. A. Suzuki, H. Tanaka, H. Yamashige, *et al.*, “Femtosecond X-ray Laser Reveals Intact Sea–Island Structures of Metastable Solid-State Electrolytes for Batteries,” *Nano Lett.* **22**, 4603–4607 (2022).
12. M. M. Seibert, T. Ekeberg, F. R. N. C. Maia, *et al.*, “Single mimivirus particles intercepted and imaged with an X-ray laser,” *Nature* **470**, 78–U86 (2011).
13. T. Gorkhover, A. Ulmer, K. Ferguson, *et al.*, “Femtosecond X-ray Fourier holography imaging of free-flying nanoparticles,” *Nat. Photonics* **12**, 150–153 (2018).
14. M. F. Hantke, D. Hasse, F. R. N. C. Maia, *et al.*, “High-throughput imaging of heterogeneous cell organelles with an X-ray laser,” *Nat. Photonics* **8**, 943–949 (2014).
15. Y. Takayama, Y. Inui, Y. Sekiguchi, *et al.*, “Coherent X-Ray Diffraction Imaging of Chloroplasts from *Cyanidioschyzon merolae* by Using X-Ray Free Electron Laser,” *Plant Cell Physiol.* **56**, 1272–1286 (2015).
16. D. Pan, J. Fan, Z. Nie, *et al.*, “Quantitative analysis of the effect of radiation on mitochondria structure using coherent diffraction imaging with a clustering algorithm,” *IUCr* **9**, 223–230 (2022).
17. T. Kimura, Y. Joti, A. Shibuya, *et al.*, “Imaging live cell in micro-liquid enclosure by X-ray laser diffraction,” *Nat. Commun.* **5**, 3052 (2014).
18. G. van der Schot, M. Svenda, F. R. N. C. Maia, *et al.*, “Imaging single cells in a beam of live cyanobacteria with an X-ray laser,” *Nat. communications* **6**, 5704 (2015).
19. A. Kobayashi, Y. Takayama, T. Hirakawa, *et al.*, “Common architectures in cyanobacteria *Prochlorococcus* cells visualized by X-ray diffraction imaging using X-ray free electron laser,” *Sci. Reports* **11**, 3877 (2021).
20. J. Garcia-Sucerquia, W. Xu, S. K. Jericho, *et al.*, “Digital in-line holographic microscopy,” *Appl. Opt.* **45**, 836 (2006).
21. T. Gorniak, R. Heine, A. P. Mancuso, *et al.*, “X-ray holographic microscopy with zone plates applied to biological samples in the water window using 3rd harmonic radiation from the free-electron laser FLASH,” *Opt. Express* **19**, 11059 (2011).
22. B. Abbey, K. A. Nugent, G. J. Williams, *et al.*, “Keyhole coherent diffractive imaging,” *Nat. Phys.* **4**, 394–398 (2008).
23. G. J. Williams, H. M. Quiney, A. G. Peele, and K. A. Nugent, “Fresnel coherent diffractive imaging: Treatment and analysis of data,” *New J. Phys.* **12**, 035020 (2010).
24. M. Vassholz, H. P. Hoeppe, J. Hagemann, *et al.*, “Pump-probe X-ray holographic imaging of laser-induced cavitation bubbles with femtosecond FEL pulses,” *Nat. Commun.* **12**, 3468 (2021).
25. J. Hagemann, M. Vassholz, H. Hoeppe, *et al.*, “Single-pulse phase-contrast imaging at free-electron lasers in the hard X-ray regime,” *J. Synchrotron Radiat.* **28**, 52–63 (2021).
26. R. L. Sandberg, C. Bolme, K. Ramos, *et al.*, “Ultrafast Imaging of Shocked Material Dynamics with X-ray Free Electron Laser Pulses,” in *CLEO: 2014 Postdeadline Paper Digest*, (OSA, San Jose, California, 2014), p. STh5C.8.
27. A. Schropp, R. Hoppe, V. Meier, *et al.*, “Imaging Shock Waves in Diamond with Both High Temporal and Spatial Resolution at an XFEL,” *Sci. reports* **5**, 11089 (2015).

28. B. Nagler, A. Schropp, E. C. Galtier, *et al.*, “The phase-contrast imaging instrument at the matter in extreme conditions endstation at LCLS,” *Rev. Sci. Instruments* **87**, 103701 (2016).
29. F. Seiboth, L. B. Fletcher, D. McGonegle, *et al.*, “Simultaneous 8.2 keV phase-contrast imaging and 24.6 keV X-ray diffraction from shock-compressed matter at the LCLS,” *Appl. Phys. Lett.* **112**, 221907 (2018).
30. P. Vagovič, T. Sato, L. Mikeš, *et al.*, “Megahertz x-ray microscopy at x-ray free-electron laser and synchrotron sources,” *Optica* **6**, 1106 (2019).
31. I. McNulty, J. Kirz, C. Jacobsen, *et al.*, “High-Resolution Imaging by Fourier Transform X-ray Holography,” *Science* **256**, 1009–1012 (1992).
32. S. Eisebitt, J. Lüning, W. F. Schlotter, *et al.*, “Lensless imaging of magnetic nanostructures by X-ray spectro-holography,” *Nature* **432**, 885–888 (2004).
33. S. Marchesini, S. Boutet, A. E. Sakdinawat, *et al.*, “Massively parallel X-ray holography,” *Nat. Photonics* **2**, 560–563 (2008).
34. M. Guizar-Sicairos and J. R. Fienup, “Direct image reconstruction from a Fourier intensity pattern using HERALDO,” *Opt. Lett.* **33**, 2668 (2008).
35. A. V. Martin, A. J. D’Alfonso, F. Wang, *et al.*, “X-ray holography with a customizable reference,” *Nat. Commun.* **5**, 4661 (2014).
36. L. Müller, S. Schleitner, C. Gutt, *et al.*, “Ultrafast Dynamics of Magnetic Domain Structures Probed by Coherent Free-Electron Laser Light,” *Synchrotron Radiat. News* **26**, 27–32 (2013).
37. F. Willems, C. von Korff Schmising, D. Weder, *et al.*, “Multi-color imaging of magnetic Co/Pt heterostructures,” *Struct. Dyn.* **4**, 014301 (2017).
38. C. von Korff Schmising, B. Pfau, M. Schneider, *et al.*, “Imaging Ultrafast Demagnetization Dynamics after a Spatially Localized Optical Excitation,” *Phys. Rev. Lett.* **112**, 217203 (2014).
39. S. Egawa, K. Sakurai, Y. Takeo, *et al.*, “Observation of mammalian living cells with femtosecond single pulse illumination generated by a soft X-ray free electron laser,” *Optica* **11**, 736 (2024).
40. A. L. Levitan, K. Keskinbora, U. T. Sanli, *et al.*, “Single-frame far-field diffractive imaging with randomized illumination,” *Opt. Express* **28**, 37103 (2020).
41. P. Sidorenko and O. Cohen, “Single-shot ptychography,” *Optica* **3**, 9–14 (2016).
42. K. Kharitonov, M. Mehrjoo, M. Ruiz-Lopez, *et al.*, “Single-shot ptychography at a soft X-ray free-electron laser,” *Sci. Reports* **12**, 14430 (2022).
43. F. Pfeiffer, “X-ray ptychography,” *Nat. Photonics* **12**, 9–17 (2018).
44. A. Levitan, M. Cain, and A. Kutakh, “CDTools 0.2.0 (python package),” (2024). <https://github.com/cdtools-developers/cdtools>.
45. P. Thibault and A. Menzel, “Reconstructing state mixtures from diffraction measurements,” *Nature* **494**, 68–71 (2013).
46. A. Tripathi, I. McNulty, and O. G. Shpyrko, “Ptychographic overlap constraint errors and the limits of their numerical recovery using conjugate gradient descent methods,” *Opt. Express* **22**, 1452 (2014).
47. S. Marchesini, A. Schirotzek, C. Yang, *et al.*, “Augmented projections for ptychographic imaging,” *Inverse Probl.* **29** (2013).
48. A. M. Maiden, M. J. Humphry, F. Zhang, and J. M. Rodenburg, “Superresolution imaging via ptychography,” *J. Opt. Soc. Am. A, Opt. image science, vision* **28**, 604–12 (2011).
49. A. Levitan, K. Keskinbora, M. Pancaldi, *et al.*, “Replication Data for: Single shot imaging with randomized structured illumination at a free electron laser,” (2026). <https://doi.org/10.7910/DVN/4LYYRS>.
50. A. Levitan and R. Comin, “Error metrics for partially coherent wave fields,” *Opt. Lett.* **47**, 2322 (2022).
51. P. A. Penczek, “Resolution Measures in Molecular Electron Microscopy,” in *Methods in Enzymology*, vol. 482 (Elsevier, 2010), pp. 73–100.
52. M. Van Heel and M. Schatz, “Fourier shell correlation threshold criteria,” *J. Struct. Biol.* **151**, 250–262 (2005).
53. J. Vila-Comamala, A. Diaz, M. Guizar-Sicairos, *et al.*, “Characterization of high-resolution diffractive X-ray optics by ptychographic coherent diffractive imaging,” *Opt. Express* **19**, 21333 (2011).
54. M. Guizar-Sicairos, M. Holler, A. Diaz, *et al.*, “Role of the illumination spatial-frequency spectrum for ptychography,” *Phys. Rev. B - Condens. Matter Mater. Phys.* **86**, 100103(R) (2012).
55. C. Donnelly, V. Scagnoli, M. Guizar-Sicairos, *et al.*, “High resolution hard x-ray magnetic imaging with dichroic ptychography,” *Phys. Rev. B* **064421**, 1–5 (2016).
56. D. A. Shapiro, S. Babin, R. S. Celestre, *et al.*, “An ultrahigh-resolution soft x-ray microscope for quantitative analysis of chemically heterogeneous nanomaterials,” *Sci. Adv.* **6**, eabc4904 (2020).
57. J. R. Fienup, “Invariant error metrics for image reconstruction,” *Appl. Opt.* **36**, 8352 (1997).
58. A. W. Lohmann, R. G. Dorsch, D. Mendlovic, *et al.*, “Space-bandwidth product of optical signals and systems,” *J. Opt. Soc. Am. A* **13**, 470 (1996).
59. A. Martin, N. Loh, C. Hampton, *et al.*, “Femtosecond dark-field imaging with an X-ray free electron laser,” *Opt. Express* **20**, 13501 (2012).
60. F. Capotondi, E. Pedersoli, N. Mahne, *et al.*, “Invited Article: Coherent imaging using seeded free-electron laser pulses with variable polarization: First results and research opportunities,” *Rev. Sci. Instruments* **84**, 051301 (2013).
61. B. Pfau, C. M. Günther, S. Schaffert, *et al.*, “Femtosecond pulse x-ray imaging with a large field of view,” *New J. Phys.* **12**, 095006 (2010).

Single-shot imaging with randomized structured illumination at a free electron laser: supplemental document

This document includes supplemental figures and detailed descriptions of the experimental methods used in the paper, "Single-shot imaging with randomized structured illumination at a free electron laser".

S1. OPTIC DESIGN AND FABRICATION

The design file for the RZP was produced using the method discussed in [1]. The design parameters were: 200 nm outer zone width; 800 μm diameter; and a focal spot diameter of 40 μm . An integrated beamstop was included with a diameter of 400 μm . The designed optic has a focal distance of 7.743 mm at the design photon energy of 60 eV. The raster design file was generated at a 50 nm resolution, with computation performed on the MIT Supercloud cluster [2].

The optic was fabricated using a dedicated ion beam lithography platform (VELION, Raith, De) [3–5]. A 250 nm thick layer of gold for the beamstop was first deposited on a 100 nm thick silicon carbide membrane window using magnetron sputtering. The 400 μm diameter beamstop was then cut out using a sketch-and-peel process [6]. A further 50 nm thick layer of gold was deposited on the chip for the RZP pattern. The optic exposure pattern was divided into 10×10 80 μm write fields. Each field was exposed using a 35 keV beam of Au⁺ ions with a current of 344 pA and a pixel size of 50 nm. The outer zone width of 200 nm was chosen to allow us to work at a low numerical aperture for this initial experiment. Images outlining the process can be found in figure S1.

S2. FEL DATA COLLECTION

Experiments were performed at the DiProI beamline of the FERMI free electron laser (FEL) [7]. FEL-1 was used, producing pulses of light at 59.6 eV with an estimated duration of 60 fs [8] and an estimated bandwidth $\frac{\Delta E}{E} > 1000$. The adjustable Kirkpatrick-Baez mirrors were underfocused, producing a beam of several millimeters in diameter at the plane of the optic. The optic was attached to an integrated mount with a matched order selecting aperture, and this mount was affixed to a set of x/y/z scanning motors and a goniometer for alignment with the optic axis.

To study the gold resolution test target, this spot was scanned over the test sample in a Fermat spiral pattern to generate a 300-shot ptychography dataset for calibration. Following that, 128 single-shot images were collected for analysis with randomized probe imaging (RPI). The diffraction was captured on a 2048×2048 CCD detector (Princeton Instruments MTE 2048B) with 13.5 μm pixels placed 135 mm downstream from the sample, run with 2×2 binning. Each single-shot diffraction pattern in the dataset used for single-shot RPI reconstructions contained an average of 1.2×10^7 detected photons, equivalent to 490 photons per 200 nm resolution element within the illuminated region. Accounting for absorption in the sample and the detector quantum efficiency, this corresponds to an estimated total pulse energy incident on the sample of 1.4 nJ, or a mean illumination fluence of $110 \mu\text{J cm}^{-2}$.

The imaging geometry, including incident fluence, was identical for the sample of Ta(3 nm) / [Pt(3 nm) / Co(1 nm) / Ta(1.9 nm)] $\times 10$ / Pt(2 nm). Due to the weaker contrast and correspondingly lower resolution, a super-resolution model was not used for analysis, and instead the detector was cropped by 100 pixels to enable a better quality background subtraction to be performed. A ptychographic dataset in a Fermat spiral pattern was collected with 200 exposures for left-hand circular light, and with 215 exposures for right-handed circular light. Due to increased absorption in the magnetic sample, each single-shot diffraction pattern in the dataset used for single-shot RPI reconstructions contained an average of only 2.8×10^6 detected photons, equivalent to 2.8×10^3 measured photons per μm^2 .

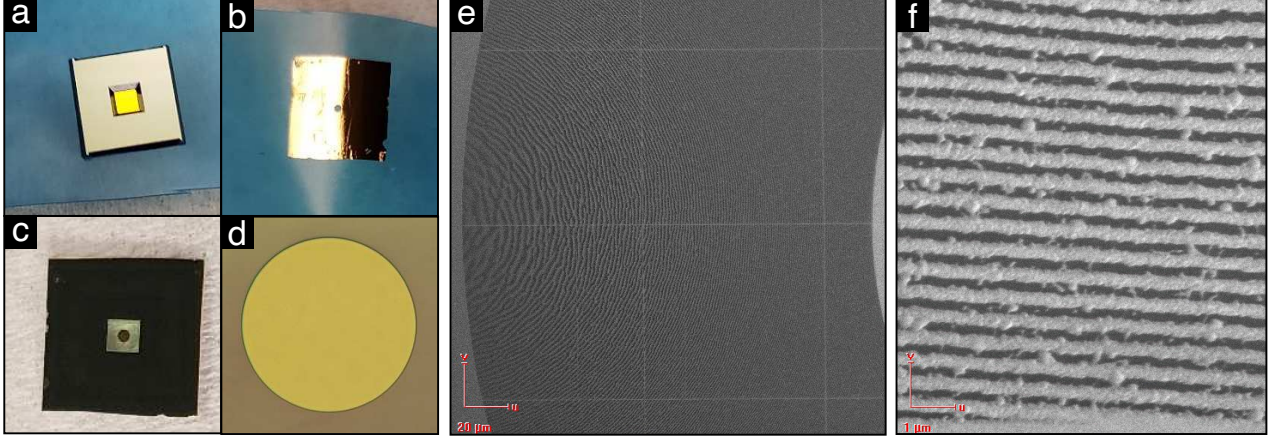


Fig. S1. Optics. (a-d), The sketch-and-peel process for defining the beamstop. After ion beam lithography milling, the membrane is brought in contact with a low-tack tape (a), leaving a residual gold layer (b) on the tape, and the beamstop (c,d) on the membrane. (e-f), scanning electron microscope images of a large area (e) and the outermost zones (f) of the final ion-beam-lithography-fabricated randomized zone plate (RZP).

S3. RESOLUTION ESTIMATION METHODOLOGY

We used the spectral signal-to-noise ratio (SSNR) to estimate the resolution of the ptychography and RPI reconstructions reported in the paper. The SSNR is a function of the Fourier ring correlation (FRC) or Fourier cross resolution (FCR) and is used as an estimator of the signal-to-noise ratio within each of the radial bands defined in the calculation of the FRC.

In the classic setting for ptychography, two reconstructions are performed, each using half of the data. An appropriate estimator for the signal to noise ratio of the combined reconstruction, defined as a function of the FRC calculated between the two half-data reconstructions, is [10, 11]:

$$\text{SSNR} = 2 \frac{\text{FRC}}{1 - \text{FRC}} \quad (\text{S1})$$

The factor of 2 arises because we are estimating the SSNR of the combined result.

However, we also want to be able to study noisy RPI images by comparing single-shot reconstructions with much less noisy ptychography results that can be treated as a ground truth image. A common estimator for the SSNR of the noisy image in this case uses the FCR, [10] and is:

$$\text{SSNR} = \frac{\text{FCR}^2}{1 - \text{FCR}^2} \quad (\text{S2})$$

In our work, we compare the estimate of the SSNR to the half-bit threshold $\text{SSNR} = 2^{0.5} - 1 \approx 0.414$, the threshold level proposed by Van Heel in the context of FRC curves [12] and most commonly used in the ptychography literature. It is more common to compare the FRC curve to one of the threshold curves defined by [12].

Here, we choose to use the SSNR to enable comparison of the the ptychography results (analyzed via FRC) and RPI results (analyzed via FCR) on the same footing. To make it clear that this has not led to a reduction in the stringency of the resolution criteria, we have also included raw FRC and FCR curves in Supplementary figures S4 and S2.

Finally, we estimated the number of measured photons per shot using the knowledge that the detector's output amplifier maps an input of 0-200,000 electrons to 16-bit output range, 0.32 analog detector units per electron. We assumed that each detected photon produced one electron per every 3.6 eV of photon energy. This leads to a final conversion of 5.4 analog detector units per detected photon.

S4. LINECUT METHODOLOGY

We took a cut from the image along a circular arc that the spokes of the Siemens star intersect at a constant pitch. Because the path doesn't follow the grid axes, some form of interpolation is

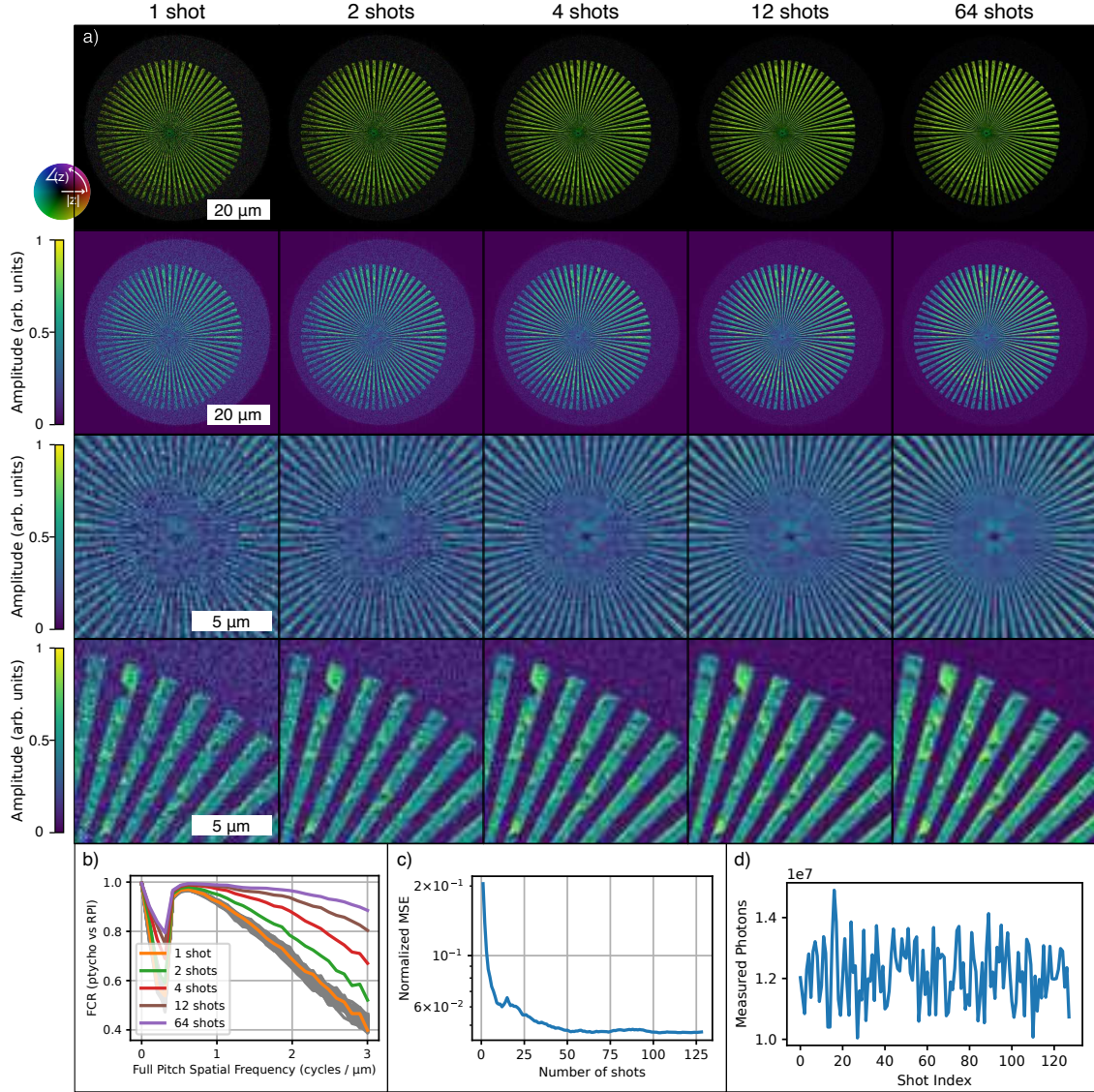


Fig. S2. Shot Number Dependence of RPI. (a) The complex-valued image, amplitude, and two zoomed regions of the sample, as synthesized from a sum of 1, 2, 4, 12, and 64 shots. (b) The FCR between each of the images above and the object, as reconstructed by ptychography. This was used to estimate the SSNR reported in the main text (c) The dependence of the overall amplitude-minimized normalized mean squared error [9] on the number of included shots, from 1 to 128. (d) The number of photons measured on the detector for each of the 128 diffraction patterns.

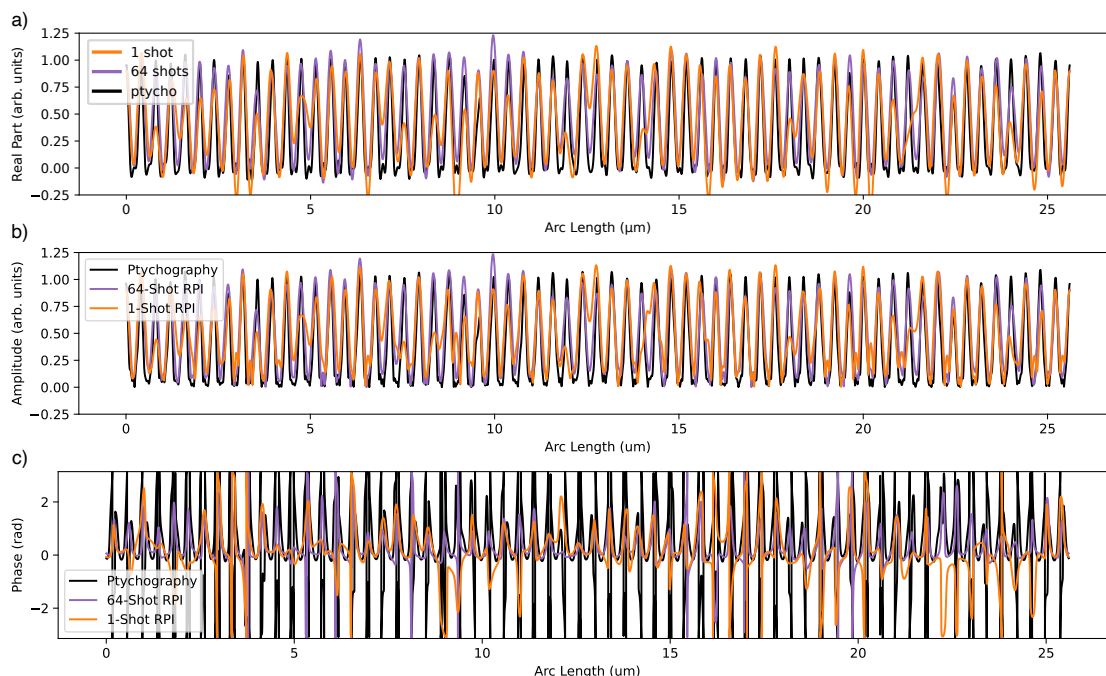


Fig. S3. Full Arc Cut. (a) The real part, (b) the amplitude, and (c) the phase of a full cut from various reconstructions of the test sample, along an arc which intersects the spokes of the Siemens star at a 400 nm pitch. Included is a linecut from the ptychography reconstruction, from a representative RPI reconstruction from one shot, and from an averaged RPI reconstruction including 64 shots of data.

required. We used a sinc-interpolation, implemented by zero-padding in Fourier space. This is a natural choice because it matches the assumption baked into the RPI model, which upsamples the low-resolution image with an identical zero-padding in Fourier space.

Once the image is sufficiently upsampled, the final linecut was extracted using a linear interpolation to sample explicit points defined along an arc. The center point of the arc's circle was identified manually.

S5. LITERATURE SEARCH

On November 13, 2023, we searched Clarivate web of science for the term:

```
(ALL=("Free Electron Laser") OR ALL=("Free Electron Lasers") OR ALL=("FEL")
OR ALL=("FELs") OR ALL=("XFEL") OR ALL=("XFELs") OR ALL=("Linac Coherent
Light Source") OR ALL=("LCLS") OR ALL=("SACLA") OR ALL=("SPring-8
Angstrom Compact free electron LAsEr") OR ALL=("SwissFEL"))
AND
(ALL=("Holography") OR ALL=("Holographic") OR ALL=("Ptychography") OR
ALL=("Ptychographic") OR ALL=("Phase Retrieval") OR ALL=("FXI") OR ALL=("CDI")
OR ALL=("CMI") OR ALL=("SSP") OR ALL=("Microscope") OR ALL=("Microscopes")
OR ALL=("Microscopy") OR ALL=("Image") OR ALL=("Images") OR ALL=("Imaging"))
```

The search term identifies papers which both mention FELs and are plausibly related to quantitative phase microscopy. We included all generic terms for free electron laser of which we are aware, as well as the commonly used acronyms for every currently operating short wavelength free electron laser. We excluded the European XFEL and the Shanghai XFEL, as both names are already captured by the search term "XFEL". "FERMI" (Free Electron laser Radiation for Multidisciplinary Investigations) and "FLASH" (Free Electron LASer in Hamburg) were also excluded because they matched an unmanageably large number of papers unrelated to FELs, and their full names are already captured by "Free Electron Laser". This search returned 5,094 results.

Our goal was to identify all FEL-based publications that produced quantitative phase images using a method compatible with single-shot operation. Therefore, we excluded papers that only reported ptychography results, e.g. [13, 14]. We did include Fourier transform holography results even when a sum over multiple shots was used (e.g. [15] or [16]). We also included in-line holography publications where phase retrieval was attempted, but excluded publications where raw phase-contrast images were reported without any quantitative inversion of the full 2D image (e.g. [17–27]).

To identify the relevant papers, we started by reading the title. For all papers which weren't obviously false positives (e.g. papers about the cat-allergy-related FEL protein), we read the abstract and viewed the figures, reading the full paper only if either the abstract or figures indicated the presence of data meeting our conditions. In cases where multiple papers used the same dataset, we only included the publication that reported the highest-quality images. In the end, we found 96 papers which reported unique quantitative phase contrast images captured by FELs [7, 15, 16, 24, 28–119].

Within each paper, we identified the image with the highest resolution and space-bandwidth product, adding multiple results if these images were not the same or if images captured with multiple methods were presented. This resulted in 101 unique images. Finally, we added one additional phased dataset [120] which had not been indexed in web of science because it was published in Synchrotron Radiation News. This brought the total to 97 papers and 102 images.

From each image, we estimated the full-pitch resolution, the field of view, and the space-bandwidth product. The resolution was calculated based on the author's claims, if possible. We accepted all author resolution claims based on image features - for example, 10%-90% rise, FRC or phase retrieval transfer function calculations, or visibility of lines in a test target. If a half-pitch resolution was reported, we converted it to full-pitch. In cases where the pixel pitch was reported as the resolution, where the resolution was derived from a numerical aperture-based argument, or no resolution was reported, we attempted to estimate the image resolution using the provided images. If the images appeared close to pixel-resolved, we simply used the pixel pitch. Otherwise, we manually estimated the length scale of the smallest features visible in the images. Because of the variety of methods used, we suggest that the resolution estimates should only be trusted to within roughly a factor of 2.

The field of view was estimated as the area of a box surrounding the imaged region. In cases where the field of view was densely populated, the space-bandwidth product was calculated using this field of view as the imaged area. In cases where the object had a narrow, sparse, or disjoint support, the actual imaged area can be an order of magnitude or more less than the area contained within this bounding box. In these cases we attempted to estimate the area of the imaged region. For cases where the object has disjoint support, the area of each disjoint region was separately estimated and then added. For circular supports, the area of the circle was calculated. Finally, in cases where a finite support constraint was used and the number of pixels in that support region was reported, the number of pixels was used to calculate the area of the field of view.

Finally, the space-bandwidth product was calculated as follows:

$$SBP = A_{\text{real}} A_{\text{Fourier}} = \pi A_{\text{real}} \text{res}^2. \quad (\text{S3})$$

Where res is expressed in cycles per length. A spreadsheet containing all the papers included in the search, as well as the resolution and field of view estimates, is available with the replication data and code at reference [121].

S6. ADDITIONAL FIGURES

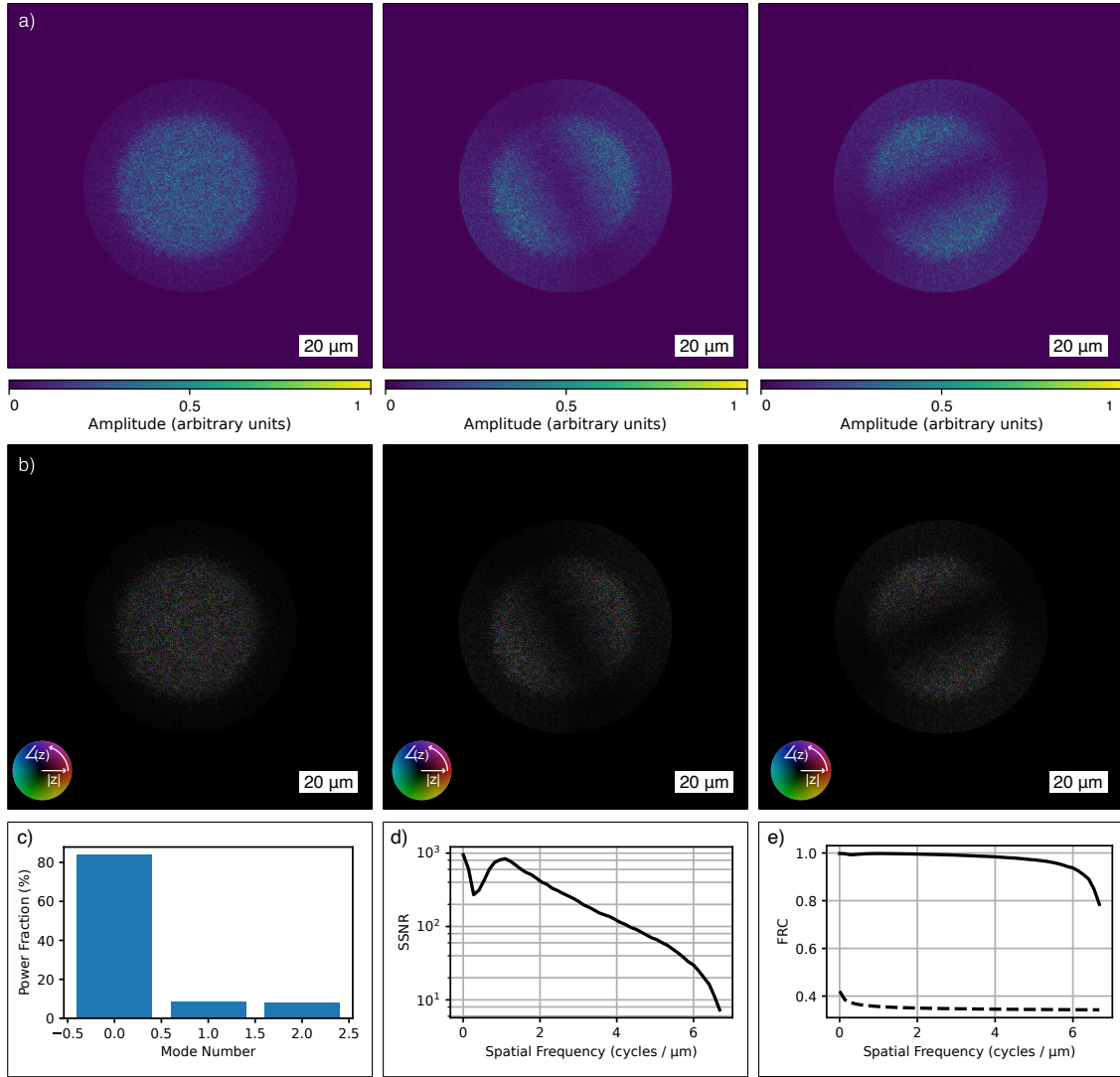


Fig. S4. Ptychography Calibration Details. (a) The amplitudes of the three reconstructed probe modes, normalized to the brightest pixel within each image. (b) The complex-valued probe modes. (c) The power ratio of the three modes. (d) The SSNR of the reconstructed object, as estimated via the FRC. (e) The FRC of the reconstructed object, compared with a half-bit threshold.

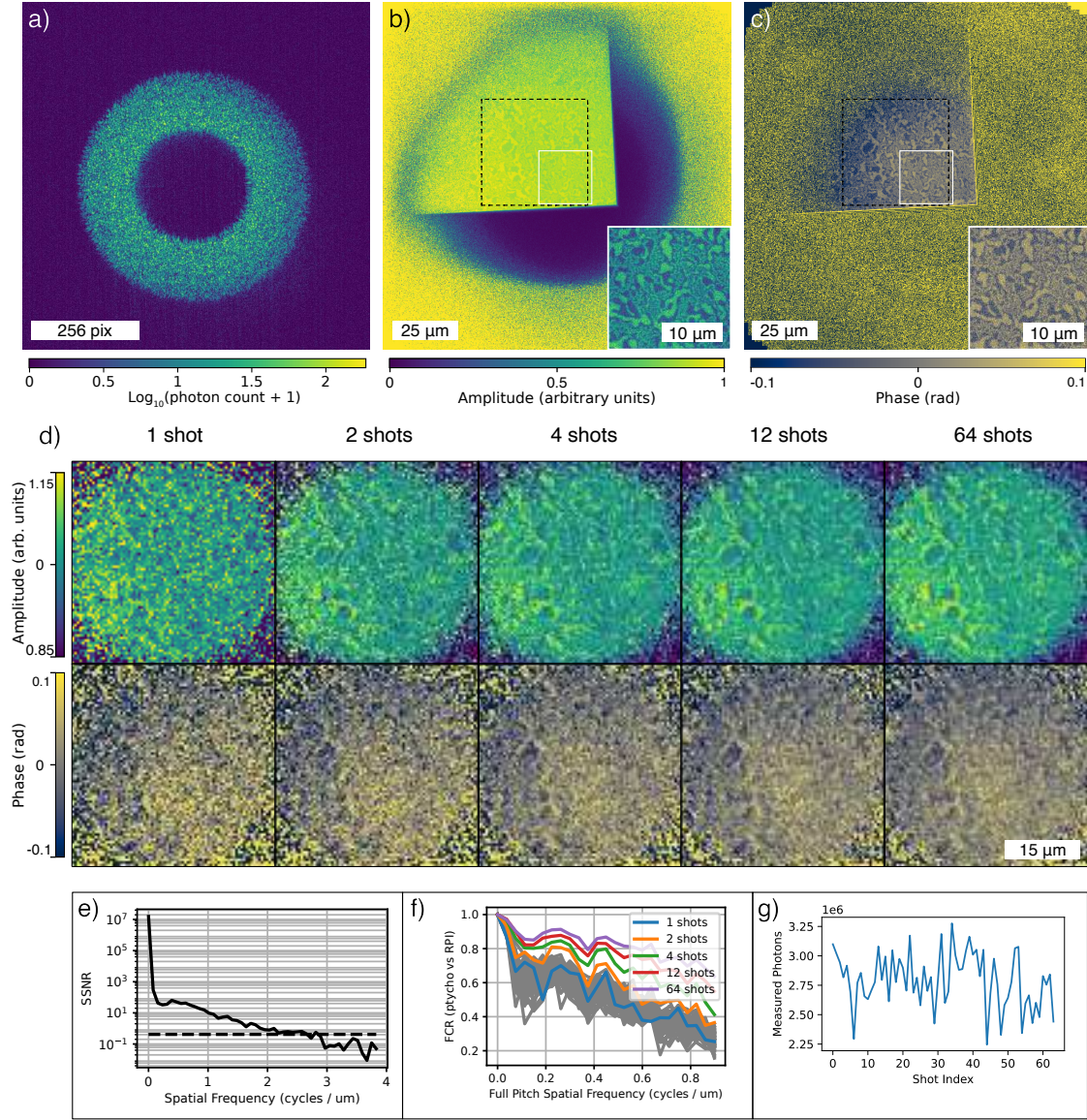


Fig. S5. Magnetic Imaging Details. (a) A representative detector image after background subtraction, used for the reported single-shot RPI reconstruction. Ptychographic amplitude (b) and phase (c) maps using left-hand circularly polarized light. The region which overlaps with the RPI reconstructions is shown in a dashed black line, and the region used for FRC calculation is outlined in white (inset). The color scale of the overview amplitude image in (b) is set to preserve the zero level, and the color scale of the inset matches that in Figure 3b from the main manuscript. (d) Shot-number dependence of the averaged RPI images. (e) SSNR, calculated via FRC, of the magnetic ptychography images. The threshold is set at 0.414 as discussed in Section S3. (f) FCR curves, calculated against the ptychography reconstruction, for each image in (d). (g) The shot-to-shot intensity of the data used for magnetic RPI.

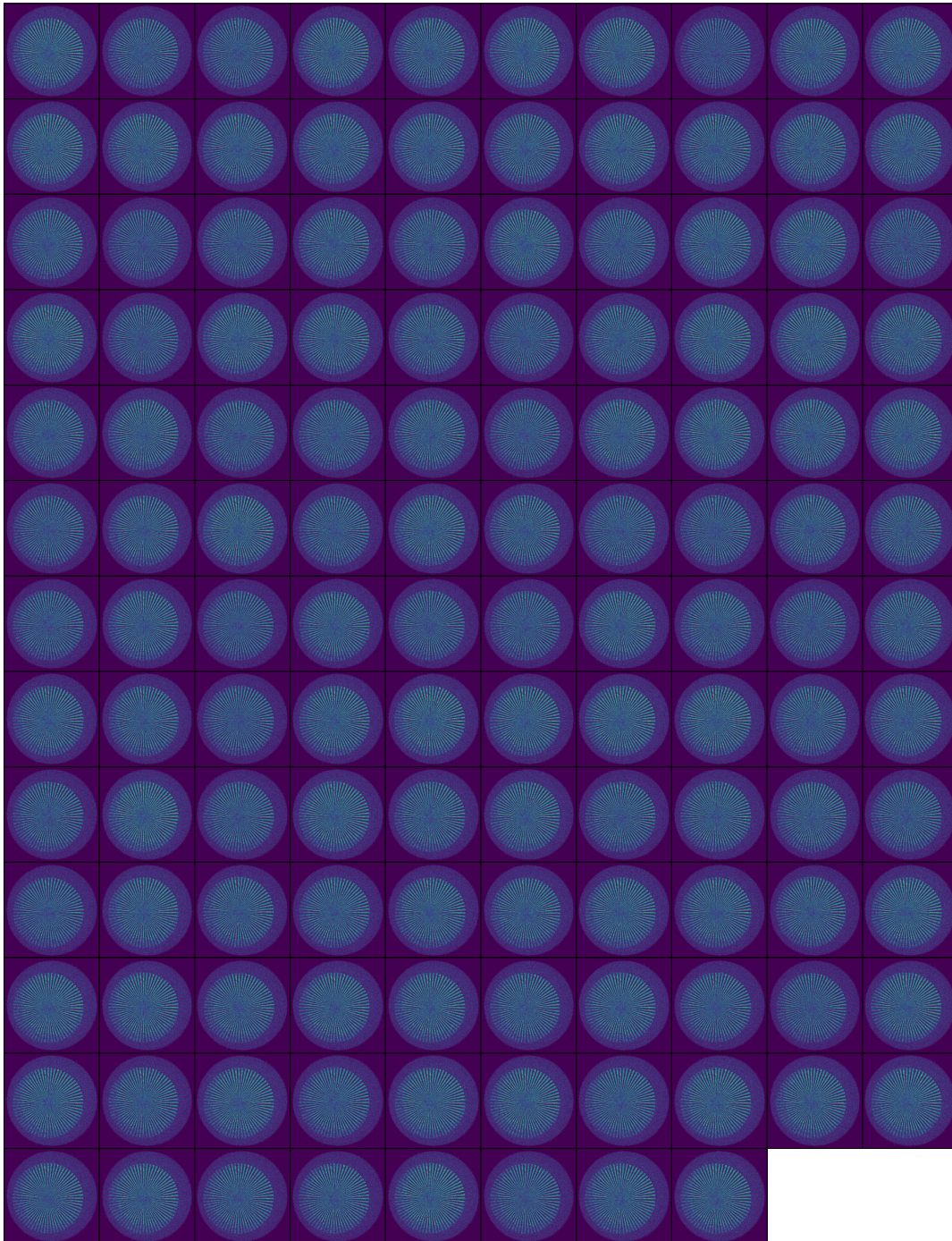


Fig. S6. All RPI Reconstructions. The amplitude of all 128 single-shot RPI reconstructions.

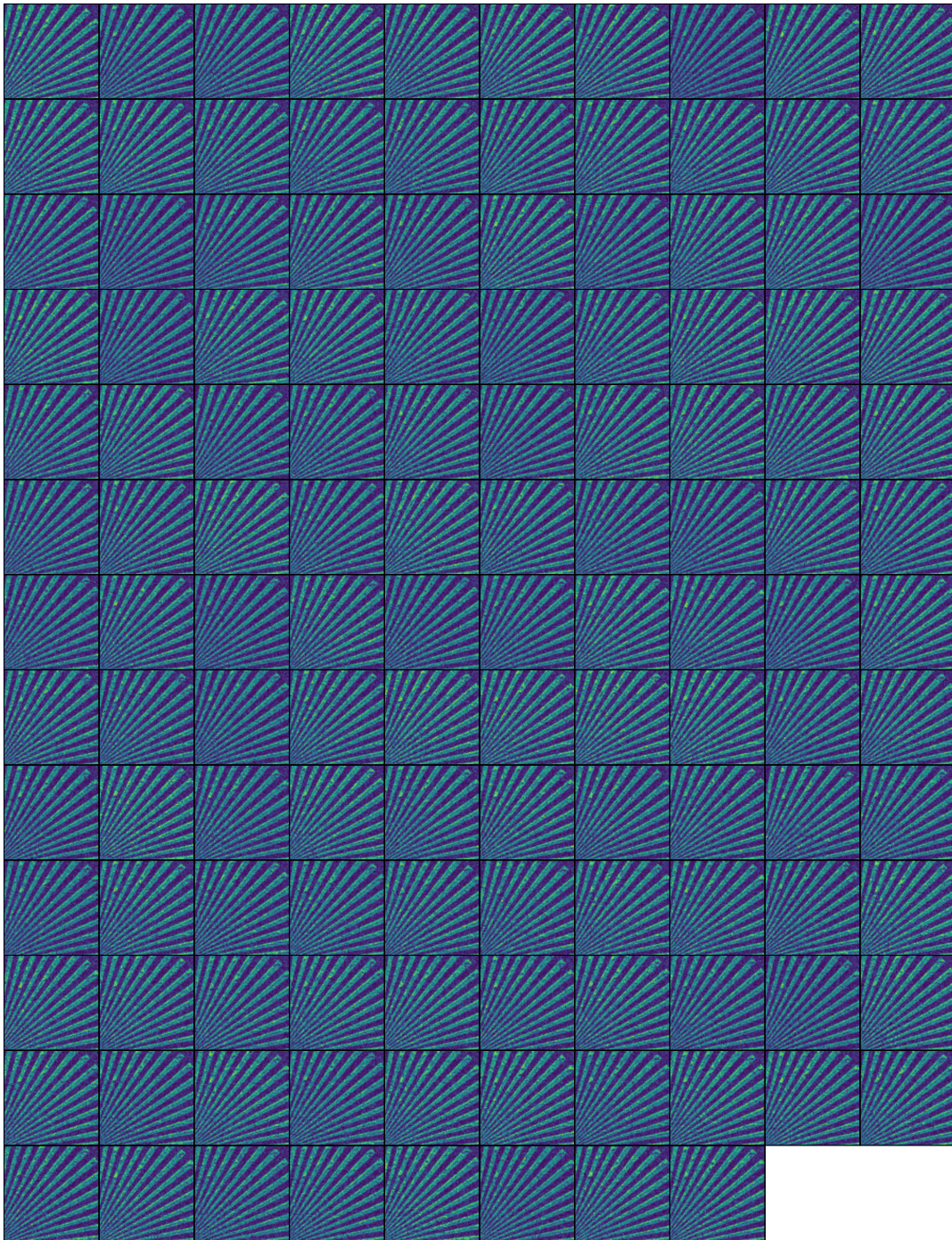


Fig. S7. Cropped RPI Reconstructions. Closeup view of the amplitude of all 128 single-shot RPI reconstructions.

REFERENCES

1. A. L. Levitan, K. Keskinbora, U. T. Sanli, *et al.*, "Single-frame far-field diffractive imaging with randomized illumination," *Opt. Express* **28**, 37103 (2020).
2. A. Reuther, J. Kepner, C. Byun, *et al.*, "Interactive supercomputing on 40,000 cores for machine learning and data analysis," in *2018 IEEE High Performance Extreme Computing Conference (HPEC)*, (IEEE, 2018), pp. 1–6.
3. A. Nadzeyka, L. Peto, S. Bauerdick, *et al.*, "Ion beam lithography for direct patterning of high accuracy large area X-ray elements in gold on membranes," *Microelectron. Eng.* **98**, 198–201 (2012).
4. K. Keskinbora, C. Grévent, U. Eigenthaler, *et al.*, "Rapid Prototyping of Fresnel Zone Plates via Direct Ga⁺ Ion Beam Lithography for High-Resolution X-ray Imaging," *ACS Nano* **7**, 9788–9797 (2013).
5. K. Keskinbora, U. T. Sanli, M. Baluktsian, *et al.*, "High-throughput synthesis of modified Fresnel zone plate arrays via ion beam lithography," *Beilstein J. Nanotechnol.* **9**, 2049–2056 (2018).
6. Y. Chen, Q. Xiang, Z. Li, *et al.*, "'Sketch and Peel' Lithography for High-Resolution Multiscale Patterning," *Nano Lett.* **16**, 3253–3259 (2016).
7. F. Capotondi, E. Pedersoli, N. Mahne, *et al.*, "Invited Article: Coherent imaging using seeded free-electron laser pulses with variable polarization: First results and research opportunities," *Rev. Sci. Instruments* **84**, 051301 (2013).
8. E. Allaria, R. Appio, L. Badano, *et al.*, "Highly coherent and stable pulses from the FERMI seeded free-electron laser in the extreme ultraviolet," *Nat. Photonics* **6**, 699–704 (2012).
9. J. R. Fienup, "Invariant error metrics for image reconstruction," *Appl. Opt.* **36**, 8352 (1997).
10. P. A. Penczek, "Resolution Measures in Molecular Electron Microscopy," in *Methods in Enzymology*, vol. 482 (Elsevier, 2010), pp. 73–100.
11. M. Unser, B. L. Trus, and A. C. Steven, "A new resolution criterion based on spectral signal-to-noise ratios," *Ultramicroscopy* **23**, 39–51 (1987).
12. M. Van Heel and M. Schatz, "Fourier shell correlation threshold criteria," *J. Struct. Biol.* **151**, 250–262 (2005).
13. B. A. Pound, K. M. Mertes, A. V. Carr, *et al.*, "Ptychography at the Linac Coherent Light Source in a parasitic geometry," *J. Appl. Crystallogr.* **53** (2020).
14. K. Kharitonov, M. Mehrjoo, M. Ruiz-Lopez, *et al.*, "Flexible ptychography platform to expand the potential of imaging at free electron lasers," *Opt. Express* **29**, 22345 (2021).
15. C. von Korff Schmising, B. Pfau, M. Schneider, *et al.*, "Imaging Ultrafast Demagnetization Dynamics after a Spatially Localized Optical Excitation," *Phys. Rev. Lett.* **112**, 217203 (2014).
16. F. Willems, C. von Korff Schmising, D. Weder, *et al.*, "Multi-color imaging of magnetic Co/Pt heterostructures," *Struct. Dyn.* **4**, 014301 (2017).
17. M. A. Beckwith, S. Jiang, A. Schropp, *et al.*, "Imaging at an x-ray absorption edge using free electron laser pulses for interface dynamics in high energy density systems," *Rev. Sci. Instruments* **88**, 053501 (2017).
18. K. Buakor, Y. Zhang, Š. Birnšteinová, *et al.*, "Shot-to-shot flat-field correction at X-ray free-electron lasers," *Opt. Express* **30**, 10633 (2022).
19. A. Y. Faenov, T. A. Pikuz, P. Mabey, *et al.*, "Advanced high resolution x-ray diagnostic for HEDP experiments," *Sci. Reports* **8**, 16407 (2018).
20. Y. Maeda, Y. Hironaka, T. Iwasaki, *et al.*, "Observation of ultra-high energy density state with x-ray free electron laser SACLA," *High Energy Density Phys.* **36**, 100813 (2020).
21. S. Makarov, S. Dyachkov, T. Pikuz, *et al.*, "Direct imaging of shock wave splitting in diamond at Mbar pressure," *Matter Radiat. at Extrem.* **8**, 066601 (2023).
22. B. Nagler, B. Arnold, G. Bouchard, *et al.*, "The Matter in Extreme Conditions instrument at the Linac Coherent Light Source," *J. Synchrotron Radiat.* **22**, 520–525 (2015).
23. B. Nagler, A. Schropp, E. C. Galtier, *et al.*, "The phase-contrast imaging instrument at the matter in extreme conditions endstation at LCLS," *Rev. Sci. Instruments* **87**, 103701 (2016).
24. R. L. Sandberg, C. Bolme, K. Ramos, *et al.*, "Ultrafast Imaging of Shocked Material Dynamics with X-ray Free Electron Laser Pulses," in *CLEO: 2014 Postdeadline Paper Digest*, (OSA, San Jose, California, 2014), p. STh5C.8.
25. H. Sawada, T. Yabuuchi, N. Higashi, *et al.*, "Ultrafast time-resolved 2D imaging of laser-driven fast electron transport in solid density matter using an x-ray free electron laser," *Rev. Sci. Instruments* **94**, 033511 (2023).
26. A. Schropp, J. Patommel, F. Seiboth, *et al.*, "Developing a platform for high-resolution phase

- contrast imaging of high pressure shock waves in matter,” in *SPIE Optical Engineering + Applications*, S. P. Moeller, M. Yabashi, and S. P. Hau-Riege, eds. (San Diego, California, USA, 2012), p. 85040F.
27. F. Seiboth, L. B. Fletcher, D. McGonegle, *et al.*, “Simultaneous 8.2 keV phase-contrast imaging and 24.6 keV X-ray diffraction from shock-compressed matter at the LCLS,” *Appl. Phys. Lett.* **112**, 221907 (2018).
 28. S. Bajt, H. N. Chapman, E. A. Spiller, *et al.*, “Camera for coherent diffractive imaging and holography with a soft-x-ray free-electron laser,” *Appl. Opt.* **47**, 1673 (2008).
 29. A. Barty, S. Boutet, M. J. Bogan, *et al.*, “Ultrafast single-shot diffraction imaging of nanoscale dynamics,” *Nat. Photonics* **2**, 415–419 (2008).
 30. J. Bielecki, M. F. Hantke, B. J. Daurer, *et al.*, “Electrospray sample injection for single-particle imaging with x-ray lasers,” *Sci. Adv.* **5**, eaav8801 (2019).
 31. M. J. Bogan, W. H. Benner, S. Boutet, *et al.*, “Single Particle X-ray Diffractive Imaging,” *Nano Lett.* **8**, 310–316 (2008).
 32. M. J. Bogan, S. Boutet, H. N. Chapman, *et al.*, “Aerosol Imaging with a Soft X-Ray Free Electron Laser,” *Aerosol Sci. Technol.* **44**, i–vi (2010).
 33. M. J. Bogan, S. Boutet, A. Barty, *et al.*, “Single-shot femtosecond x-ray diffraction from randomly oriented ellipsoidal nanoparticles,” *Phys. Rev. Special Top. - Accel. Beams* **13**, 094701 (2010).
 34. S. Boutet, M. J. Bogan, A. Barty, *et al.*, “Ultrafast soft X-ray scattering and reference-enhanced diffractive imaging of weakly scattering nanoparticles,” *J. Electron Spectrosc. Relat. Phenom.* **166–167**, 65–73 (2008).
 35. G. Brändén, G. Hammarin, R. Harimoorthy, *et al.*, “Coherent diffractive imaging of microtubules using an X-ray laser,” *Nat. Commun.* **10**, 2589 (2019).
 36. H. N. Chapman, A. Barty, M. J. Bogan, *et al.*, “Femtosecond diffractive imaging with a soft-X-ray free-electron laser,” *Nat. Phys.* **2**, 839–843 (2006).
 37. J. N. Clark, L. Beitra, G. Xiong, *et al.*, “Imaging transient melting of a nanocrystal using an X-ray laser,” *Proc. National Acad. Sci.* **112**, 7444–7448 (2015).
 38. B. J. Daurer, K. Okamoto, J. Bielecki, *et al.*, “Experimental strategies for imaging bioparticles with femtosecond hard X-ray pulses,” *IUCrJ* **4**, 251–262 (2017).
 39. J. Diao, M. Cherukara, R. Harder, *et al.*, “Unusual Breathing Behavior of Optically Excited Barium Titanate Nanocrystals,” *Crystals* **10**, 365 (2020).
 40. J. Fan, Z. Sun, Y. Wang, *et al.*, “Single-pulse enhanced coherent diffraction imaging of bacteria with an X-ray free-electron laser,” *Sci. Reports* **6**, 34008 (2016).
 41. J.-D. Fan, Y.-J. Tong, Y.-G. Nie, *et al.*, “First commissioning results of the coherent scattering and imaging endstation at the Shanghai soft X-ray free-electron laser facility,” *Nucl. Sci. Tech.* **33**, 114 (2022).
 42. A. J. Feinberg, F. Laimer, R. M. P. Tanyag, *et al.*, “X-ray diffractive imaging of highly ionized helium nanodroplets,” *Phys. Rev. Res.* **4**, L022063 (2022).
 43. M. Gallagher-Jones, Y. Bessho, S. Kim, *et al.*, “Macromolecular structures probed by combining single-shot free-electron laser diffraction with synchrotron coherent X-ray imaging,” *Nat. Commun.* **5**, 3798 (2014).
 44. Z. Gao, J. Fan, Y. Tong, *et al.*, “Single-pulse characterization of the focal spot size of X-ray free-electron lasers using coherent diffraction imaging,” *J. Synchrotron Radiat.* **30**, 505–513 (2023).
 45. T. Gorkhover, A. Ulmer, K. Ferguson, *et al.*, “Femtosecond X-ray Fourier holography imaging of free-flying nanoparticles,” *Nat. Photonics* **12**, 150–153 (2018).
 46. T. Gorniak, R. Heine, A. P. Mancuso, *et al.*, “X-ray holographic microscopy with zone plates applied to biological samples in the water window using 3rd harmonic radiation from the free-electron laser FLASH,” *Opt. Express* **19**, 11059 (2011).
 47. C. M. Günther, B. Pfau, R. Mitzner, *et al.*, “Sequential femtosecond X-ray imaging,” *Nat. Photonics* **5**, 99–102 (2011).
 48. J. Hagemann, M. Vassholz, H. Hoeppe, *et al.*, “Single-pulse phase-contrast imaging at free-electron lasers in the hard X-ray regime,” *J. Synchrotron Radiat.* **28**, 52–63 (2021).
 49. N. Z. Hagström, M. Schneider, N. Kerber, *et al.*, “Megahertz-rate Ultrafast X-ray Scattering and Holographic Imaging at the European XFEL,” arXiv:2201.06350 [cond-mat, physics:physics] (2022).
 50. M. F. Hantke, D. Hasse, F. R. N. C. Maia, *et al.*, “High-throughput imaging of heterogeneous cell organelles with an X-ray laser,” *Nat. Photonics* **8**, 943–949 (2014).

51. S. P. Hau-Riege, S. Boutet, A. Barty, *et al.*, "Sacrificial Tamper Slows Down Sample Explosion in FLASH Diffraction Experiments," *Phys. Rev. Lett.* **104**, 064801 (2010).
52. D. S. Hodge, A. F. T. Leong, S. Pandolfi, *et al.*, "Multi-frame, ultrafast, x-ray microscope for imaging shockwave dynamics," *Opt. Express* **30**, 38405 (2022).
53. C.-F. Huang, K. S. Liang, T.-L. Hsu, *et al.*, "Free-electron-laser coherent diffraction images of individual drug-carrying liposome particles in solution," *Nanoscale* **10**, 2820–2824 (2018).
54. C.-F. Huang, W.-H. Chang, T.-K. Lee, *et al.*, "XFEL coherent diffraction imaging for weakly scattering particles using heterodyne interference," *AIP Adv.* **10**, 055219 (2020).
55. Y. Ihm, D. H. Cho, D. Sung, *et al.*, "Direct observation of picosecond melting and disintegration of metallic nanoparticles," *Nat. Commun.* **10**, 2411 (2019).
56. A. S. Johnson, D. Perez-Salinas, K. M. Siddiqui, *et al.*, "Ultrafast X-ray imaging of the light-induced phase transition in VO₂," *Nat. Phys.* (2022).
57. C. F. Jones, C. Bernando, R. M. P. Tanyag, *et al.*, "Coupled motion of Xe clusters and quantum vortices in He nanodroplets," *Phys. Rev. B* **93**, 180510 (2016).
58. C. Jung, D. Nam, J. Hwang, *et al.*, "Structural Investigation of Single Specimens with a Femtosecond X-Ray Laser: Routes to Signal-to-Noise Ratio Enhancement," *Phys. Rev. Appl.* **13**, 064045 (2020).
59. C. Jung, Y. Ihm, D. H. Cho, *et al.*, "Inducing thermodynamically blocked atomic ordering via strongly driven nonequilibrium kinetics," *Sci. Adv.* **7**, eabj8552 (2021).
60. H. Kameda, S. Usugi, M. Kobayashi, *et al.*, "Common structural features of toxic intermediates from α -synuclein and GroES fibrillogenesis detected using cryogenic coherent X-ray diffraction imaging," *J. Biochem.* **161**, 55–65 (2017).
61. J. Kang, J. Carnis, D. Kim, *et al.*, "Time-resolved in situ visualization of the structural response of zeolites during catalysis," *Nat. Commun.* **11**, 5901 (2020).
62. S. Kassemeyer, J. Steinbrener, L. Lomb, *et al.*, "Femtosecond free-electron laser x-ray diffraction data sets for algorithm development," *Opt. Express* **20**, 4149 (2012).
63. K. Kharitonov, M. Mehrjoo, M. Ruiz-Lopez, *et al.*, "Single-shotptychography at a soft X-ray free-electron laser," *Sci. Reports* **12**, 14430 (2022).
64. T. Kimura, Y. Joti, A. Shibuya, *et al.*, "Imaging live cell in micro-liquid enclosure by X-ray laser diffraction," *Nat. Commun.* **5**, 3052 (2014).
65. T. Kimura, A. Suzuki, Y. Yang, *et al.*, "Micro-liquid enclosure array and its semi-automated assembling system for x-ray free-electron laser diffractive imaging of samples in solution," *Rev. Sci. Instruments* **91**, 083706 (2020).
66. A. Kobayashi, Y. Sekiguchi, Y. Takayama, *et al.*, "Dark-field phase retrieval under the constraint of the Friedel symmetry in coherent X-ray diffraction imaging," *Opt. Express* **22**, 27892 (2014).
67. A. Kobayashi, Y. Takayama, T. Hirakawa, *et al.*, "Common architectures in cyanobacteria Prochlorococcus cells visualized by X-ray diffraction imaging using X-ray free electron laser," *Sci. Reports* **11**, 3877 (2021).
68. S. Y. Lee, D. H. Cho, C. Jung, *et al.*, "Denoising low-intensity diffraction signals using k-space deep learning: Applications to phase recovery," *Phys. Rev. Res.* **3**, 043066 (2021).
69. N. D. Loh, C. Y. Hampton, A. V. Martin, *et al.*, "Fractal morphology, imaging and mass spectrometry of single aerosol particles in flight," *Nature* **486**, 513–517 (2012).
70. A. P. Mancuso, A. Schropp, B. Reime, *et al.*, "Coherent-Pulse 2D Crystallography Using a Free-Electron Laser X-Ray Source," *Phys. Rev. Lett.* **102**, 035502 (2009).
71. A. P. Mancuso, T. Gorniak, F. Staier, *et al.*, "Coherent imaging of biological samples with femtosecond pulses at the free-electron laser FLASH," *New J. Phys.* **12**, 035003 (2010).
72. S. Marchesini, S. Boutet, A. E. Sakdinawat, *et al.*, "Massively parallel X-ray holography," *Nat. Photonics* **2**, 560–563 (2008).
73. A. V. Martin, J. Andreasson, A. Aquila, *et al.*, "Single particle imaging with soft x-rays at the Linac Coherent Light Source," in *SPIE Optics + Optoelectronics*, T. Tschentscher and D. Cocco, eds. (Prague, Czech Republic, 2011), p. 807809.
74. A. Martin, N. Loh, C. Hampton, *et al.*, "Femtosecond dark-field imaging with an X-ray free electron laser," *Opt. Express* **20**, 13501 (2012).
75. A. V. Martin, F. Wang, N. D. Loh, *et al.*, "Noise-robust coherent diffractive imaging with a single diffraction pattern," *Opt. Express* **20**, 16650 (2012).
76. A. V. Martin, A. J. D'Alfonso, F. Wang, *et al.*, "X-ray holography with a customizable reference," *Nat. Commun.* **5**, 4661 (2014).
77. Y. Matsumoto, Y. Takeo, S. Egawa, *et al.*, "An arrayed-window microfluidic device for

- observation of mixed nanoparticles with an X-ray free-electron laser," *Opt. Rev.* **29**, 7–12 (2022).
78. M. Nakasako, Y. Takayama, T. Oroguchi, *et al.*, "KOTOBUKI-1 apparatus for cryogenic coherent X-ray diffraction imaging," *Rev. Sci. Instruments* **84**, 093705 (2013).
 79. D. Nam, C. Kim, Y. Kim, *et al.*, "Fixed target single-shot imaging of nanostructures using thin solid membranes at SACLA," *J. Phys. B: At. Mol. Opt. Phys.* **49**, 034008 (2016).
 80. Y. Nishino, Y. Tanaka, M. Okada, *et al.*, "Femtosecond Snapshot Holography with Extended Reference Using Extreme Ultraviolet Free-Electron Laser," *Appl. Phys. Express* **3**, 102701 (2010).
 81. T. Nishiyama, A. Niozu, C. Bostedt, *et al.*, "Refinement for single-nanoparticle structure determination from low-quality single-shot coherent diffraction data," *IUCrJ* **7**, 10–17 (2020).
 82. T. Oroguchi, Y. Sekiguchi, A. Kobayashi, *et al.*, "Cryogenic coherent x-ray diffraction imaging for biological non-crystalline particles using the KOTOBUKI-1 diffraction apparatus at SACLA," *J. Phys. B: At. Mol. Opt. Phys.* **48**, 184003 (2015).
 83. T. Oroguchi, T. Yoshidome, T. Yamamoto, and M. Nakasako, "Growth of Cuprous Oxide Particles in Liquid-Phase Synthesis Investigated by X-ray Laser Diffraction," *Nano Lett.* **18**, 5192–5197 (2018).
 84. M. Osterhoff, M. Vassholz, H. P. Hoeppe, *et al.*, "Nanosecond timing and synchronization scheme for holographic pump–probe studies at the MID instrument at European XFEL," *J. Synchrotron Radiat.* **28**, 987–994 (2021).
 85. D. Pan, J. Fan, Z. Nie, *et al.*, "Quantitative analysis of the effect of radiation on mitochondria structure using coherent diffraction imaging with a clustering algorithm," *IUCrJ* **9**, 223–230 (2022).
 86. H. J. Park, N. D. Loh, R. G. Sierra, *et al.*, "Toward unsupervised single-shot diffractive imaging of heterogeneous particles using X-ray free-electron lasers," *Opt. Express* **21**, 28729 (2013).
 87. E. Pedersoli, N. D. Loh, F. Capotondi, *et al.*, "Mesoscale morphology of airborne core–shell nanoparticle clusters: X-ray laser coherent diffraction imaging," *J. Phys. B: At. Mol. Opt. Phys.* **46**, 164033 (2013).
 88. B. Pfau, C. M. Günther, S. Schaffert, *et al.*, "Femtosecond pulse x-ray imaging with a large field of view," *New J. Phys.* **12**, 095006 (2010).
 89. A. Rosenhahn, F. Staier, T. Nisius, *et al.*, "Digital In-line Holography with femtosecond VUV radiation provided by the free-electron laser FLASH," *Opt. Express* **17**, 8220 (2009).
 90. A. Schropp, R. Hoppe, V. Meier, *et al.*, "Imaging Shock Waves in Diamond with Both High Temporal and Spatial Resolution at an XFEL." *Sci. reports* **5**, 11089 (2015).
 91. M. Seibert, S. Boutet, M. Svenda, *et al.*, "Femtosecond diffractive imaging of biological cells," *J. Phys. B: At. Mol. Opt. Phys.* **43**, 194015 (2010).
 92. M. M. Seibert, T. Ekeberg, F. R. N. C. Maia, *et al.*, "Single mimivirus particles intercepted and imaged with an X-ray laser," *Nature* **470**, 78–U86 (2011).
 93. Y. Sekiguchi, T. Oroguchi, Y. Takayama, and M. Nakasako, "Data processing software suite *SITENNO* for coherent X-ray diffraction imaging using the X-ray free-electron laser SACLA," *J. Synchrotron Radiat.* **21**, 600–612 (2014).
 94. Y. Sekiguchi, T. Oroguchi, and M. Nakasako, "Classification and assessment of retrieved electron density maps in coherent X-ray diffraction imaging using multivariate analysis," *J. Synchrotron Radiat.* **23**, 312–323 (2016).
 95. Y. Sekiguchi, S. Hashimoto, A. Kobayashi, *et al.*, "A protocol for searching the most probable phase-retrieved maps in coherent X-ray diffraction imaging by exploiting the relationship between convergence of the retrieved phase and success of calculation," *J. Synchrotron Radiat.* **24**, 1024–1038 (2017).
 96. J. Shin, C. Jung, Y. Ihm, *et al.*, "Ultrafast Energy Transfer Process in Confined Gold Nanospheres Revealed by Femtosecond X-ray Imaging and Diffraction," *Nano Lett.* **23**, 1481–1488 (2023).
 97. C. Song, K. Tono, J. Park, *et al.*, "Multiple application X-ray imaging chamber for single-shot diffraction experiments with femtosecond X-ray laser pulses," *J. Appl. Crystallogr.* **47**, 188–197 (2014).
 98. Z. Sun, J. Fan, H. Li, *et al.*, "Necessary Experimental Conditions for Single-Shot Diffraction Imaging of DNA-Based Structures with X-ray Free-Electron Lasers," *ACS Nano* **12**, 7509–7518 (2018).
 99. D. Sung, D. Nam, M.-j. Kim, *et al.*, "Single-Shot Coherent X-ray Imaging Instrument at PAL-XFEL," *Appl. Sci.* **11**, 5082 (2021).

100. A. Suzuki, T. Kimura, Y. Yang, *et al.*, "Design of a liquid cell toward three-dimensional imaging of unidirectionally-aligned particles in solution using X-ray free-electron lasers," *Phys. Chem. Chem. Phys.* **22**, 2622–2628 (2020).
101. A. Suzuki, H. Tanaka, H. Yamashige, *et al.*, "Femtosecond X-ray Laser Reveals Intact Sea-Island Structures of Metastable Solid-State Electrolytes for Batteries," *Nano Lett.* **22**, 4603–4607 (2022).
102. Y. Takahashi, A. Suzuki, N. Zettsu, *et al.*, "Coherent Diffraction Imaging Analysis of Shape-Controlled Nanoparticles with Focused Hard X-ray Free-Electron Laser Pulses," *Nano Lett.* **13**, 6028–6032 (2013).
103. Y. Takayama, Y. Inui, Y. Sekiguchi, *et al.*, "Coherent X-Ray Diffraction Imaging of Chloroplasts from *Cyanidioschyzon merolae* by Using X-Ray Free Electron Laser," *Plant Cell Physiol.* **56**, 1272–1286 (2015).
104. Y. Takayama and K. Yonekura, "Cryogenic coherent X-ray diffraction imaging of biological samples at SACLA: A correlative approach with cryo-electron and light microscopy," *Acta Crystallogr. Sect. A Found. Adv.* **72**, 179–189 (2016).
105. R. M. P. Tanyag, C. Bernando, C. F. Jones, *et al.*, "Communication: X-ray coherent diffractive imaging by immersion in nanodroplets," *Struct. Dyn.* **2**, 051102 (2015).
106. A. Ulmer, A. Heilrath, B. Senfftleben, *et al.*, "Generation of Large Vortex-Free Superfluid Helium Nanodroplets," *Phys. Rev. Lett.* **131**, 076002 (2023).
107. P. Vagovič, T. Sato, L. Mikeš, *et al.*, "Megahertz x-ray microscopy at x-ray free-electron laser and synchrotron sources," *Optica* **6**, 1106 (2019).
108. G. van der Schot, M. Svenda, F. R. N. C. Maia, *et al.*, "Imaging single cells in a beam of live cyanobacteria with an X-ray laser." *Nat. communications* **6**, 5704 (2015).
109. M. Vassholz, H. P. Hoeppe, J. Hagemann, *et al.*, "Pump-probe X-ray holographic imaging of laser-induced cavitation bubbles with femtosecond FEL pulses," *Nat. Commun.* **12**, 3468 (2021).
110. M. Vassholz, H. P. Hoeppe, J. Hagemann, *et al.*, "Structural dynamics of water in a supersonic shockwave," *Phys. Fluids* **35**, 016126 (2023).
111. T. Wang, D. Zhu, B. Wu, *et al.*, "Femtosecond Single-Shot Imaging of Nanoscale Ferromagnetic Order in Co / Pd Multilayers Using Resonant X-Ray Holography," *Phys. Rev. Lett.* **108**, 267403 (2012).
112. D. Weder, C. Von Korff Schmising, F. Willems, *et al.*, "Multi-Color Imaging of Magnetic Co/Pt Multilayers," *IEEE Trans. on Magn.* **53**, 1–5 (2017).
113. J. Wei, K. Niikura, T. Higuchi, *et al.*, "Yolk/Shell Assembly of Gold Nanoparticles by Size Segregation in Solution," *J. Am. Chem. Soc.* **138**, 3274–3277 (2016).
114. Y. Xian, H. Liu, X. Tai, and Y. Wang, "Variance-Reduced Randomized Kaczmarz Algorithm In Xfel Single-Particle Imaging Phase Retrieval," in *2022 IEEE International Conference on Image Processing (ICIP)*, (IEEE, Bordeaux, France, 2022), pp. 3186–3190.
115. J.-H. Yang, N.-J. Chen, Y. Hwu, and C.-C. Chen, "Algorithm for characterizing the subcellular structures of nanometer-sized biological specimens in a solution using x-ray free-electron lasers," *Phys. Rev. Mater.* **3**, 123803 (2019).
116. C. H. Yoon, M. Barthelmess, R. J. Bean, *et al.*, "Conformation sequence recovery of a non-periodic object from a diffraction-before-destruction experiment," *Opt. Express* **22**, 8085 (2014).
117. R. Yoshida, H. Yamashige, M. Miura, *et al.*, "Extending the potential of x-ray free-electron lasers to industrial applications—an initiatory attempt at coherent diffractive imaging on car-related nanomaterials," *J. Phys. B: At. Mol. Opt. Phys.* **48**, 244008 (2015).
118. H. Yumoto, T. Koyama, A. Suzuki, *et al.*, "High-fluence and high-gain multilayer focusing optics to enhance spatial resolution in femtosecond X-ray laser imaging," *Nat. Commun.* **13**, 5300 (2022).
119. Y. Zhuang, S. Awel, A. Barty, *et al.*, "Unsupervised learning approaches to characterizing heterogeneous samples using X-ray single-particle imaging," *IUCrJ* **9**, 204–214 (2022).
120. L. Müller, S. Schleiter, C. Gutt, *et al.*, "Ultrafast Dynamics of Magnetic Domain Structures Probed by Coherent Free-Electron Laser Light," *Synchrotron Radiat. News* **26**, 27–32 (2013).
121. A. Levitan, K. Keskinbora, M. Pancaldi, *et al.*, "Replication Data for: Single shot imaging with randomized structured illumination at a free electron laser," (2026). <https://doi.org/10.7910/DVN/4LYYRS>.